UNIVERSITÀ DEGLI STUDI DI PADOVA

DIPARTIMENTO DI SCIENZE DEL FARMACO

CORSO DI LAUREA SPECIALISTICA IN

CHIMICA E TECNOLOGIA FARMACEUTICHE

TESI DI LAUREA

DESIGN OF POLYMER-BASED NANOPARTICLES FOR THE LOCAL TREATMENT OF GLIOBLASTOMA

RELATORE: PROF. ALESSIO MALFANTI

LAUREANDA: ANNA BOLZAN

ANNO ACCADEMICO 2023/2024

Ai miei nipoti,

vi auguro di non avere mai paura

di ripercorrere i vostri passi e riscrivere un altro cammino

per inseguire i vostri sogni.

Contents

List of Abbreviations

APCs	Antigen Presenting Cells
BBB	Blood-Brain Barrier
BCNU	Bis-chloroethylnitrosourea
CARs	Chimeric Antigen Receptors
CDKN2A	Cyclin-Dependent Kinase Inhibitor 2A
CED	Convection-Enhanced Delivery
CL GBM	Classical Glioblastoma
CL HAPLL NPs	Crosslinked Nanoparticels composed by Hyaluronic Acid and Poly-L-Lysine
CNS	Central Nervous System
CSF	Cerebral Spinal Fluid
CPE	Cell-Penetrating Enhancers
Cryo-TEM	Cryogenic Transmission Electron Microscopy
DCC	Dicyclohexyl carbodiimide
DLS	Dynamic Light Scattering
DMAP	4-(Dimethylamino)pyridine
DMTMM	4-(4,6-Dimethoxy,1,3,5-triazin-2-yl)-4-methylmorpholinium chloride
ECM	Extracellular Matrix
EGFR	epidermal growth factor receptor
EPR	Enhanced Permeability and Retention
FDA	Food and Drug Administration
GBM	Glioblastoma
GLM	Glioma
GSCs	Glioblastoma-associated Stem Cells
HA	Hyaluronic Acid
HA-PD	Hyaluronic Acid-Pyridyl Disulfide Cisteamine
HA-PD-Tz	Hyaluronic Acid-Pyridyl Disulfide Cisteamine-Tetrazine
HA-PD-Tz-PTX	Hyaluronic Acid-Pyridyl Disulfide Cisteamine-Tetrazine-Paclitaxel
HA-Tz	Hyaluronic Acid-Tetrazine
HAPLL NPs	Nanoparticles based on Hyaluronic acid and Poly-L-Lysine
IDH1	Isocitrate Dehydrogenase 1
IDH2	Isocitrate Dehydrogenase 2
IL13Rα2	Interleukin-13 Receptor Subunit Alpha-2

IL-6	Interleukin-6
IL-10	Interleukin-10
MGMT	*O^6-methylguanine-DNA methyltransferase*
MDSCs	Myeloid-Derived Suppressor Cells
MES GBM	Mesenchymal Glioblastoma
MS	Mass Spectrometry
NCCN	National Comprehensive Cancer Network
NHS-TCO	Trans-Cyclooctene succinimidyl carbonate
NL GBM	Nueral Glioblastoma
NK	Natural Killer Cells
NMR	Nuclear Magnetic Resonance
NPs	Nanoparticles
OS	Overall Survival
PBS	Phosphate Buffered Saline
PCL	Poly(ε-CaproLactone)
PD	Pyridyl Disulfide Cysteamine ·HCl salt
PDGF	Platelet-Derived Growth Factor
PDGFR	Platelet-Derived Growth Factor Receptor
PD-L1	Programmed Death-Ligand 1
PGE2	Prostaglandin E2
PGA	Poly(Glutamic Acid)
PLA	Poly(Lactic Acid)
PLL	Poly-L-Lysine
PLL-TCO	Poly-L-Lysine conjugated with Trans Cyclooctene
PNPs	Polymer Nanoparticles
PN GBM	Proneural Glioblastoma
PTX	Paclitaxel
PTX-SH	Paclitaxel modified with a thiol group
RT	Room Temperature
SA	Sialic Acid
SOC	Standard of Care
TAMs	Tumor-Associated Macrophages
TAAs	Tumor-Associated Antigens
TEM	Transmission Electrons Microscopy

TGF- β	Transforming Growth Factor β
TIME	Tumor Immunosuppressive MicroEnvironment
TILs	Tumor-Infiltrating Lymphocytes
TMZ	Temozolomide
TME	Tumor MicroEnvironment
Tregs	Regulatory T Cells
TTF	Tumor Treating Fields
Tz	Methyltetrazine-benzylamine·HCl
WHO	World Health Organization

Abstract

Glioblastoma, a grade 4 glioma, is the most common primary malignant brain tumor in adults. It represents a significant unmet clinical need with a median survival of 14-16 months. The standard of care has remained largely unchanged since 2005 (Stupp Protocol), consisting in surgical resection followed by radiation and systemic chemotherapy with temozolomide combined with corticosteroids.

Resistance to current practices is due to several factors, including the blood-brain barrier (BBB), which hinders drug passages and delivery after systemic administration, high patient-to-patient GBM intra- and inter heterogenicity, and tumor capacity to develop drug resistance.

This study proposes the development of a brain-penetrating polymeric drug delivery system that will drive the conjugated anticancer drug Paclitaxel (PTX), after local administration. By employing nanocarriers composed of crosslinked Hyaluronic Acid (HA) and Poly-L-Lysine (PLL), this nanocarrier aims to improve GBM drug infiltration.

HA (100 kDa), due to its similarity with native extracellular matrix (ECM), offers safety and biodegradability, while its low molecular weight variant exhibits potential for immune modulation through interaction with GBM and immune cells. PLL (8.2 kDa), due to its positive charges, facilitates internalization within the brain's complex architecture.

Nanoparticles are assembled using a microfluidic-based system, through the interaction between the opposite charges of HA and PLL. Additionally, the two polymers are conjugated with biorthogonal linkers, ensuring the stability of the nanoparticles in a physiological environment. The nanoparticles were fully chemically-physically analyzed using ^{1}H-NMR, Dynamic Light Scattering (to investigate their size and their zeta potential), and TEM among others to obtain a comprehensive characterization. Preliminary in vitro studies of the novel nanoparticles have been performed on murine SB28 GBM cells.

Finally, after assessing IC_{50} on the SB28 glioblastoma murine cell line, PTX has been conjugated to the nanoparticles with a bioresponsive linker and the novel nanomedicine has been fully chemically-physically characterized. The therapeutic potential of this novel nanoplatform warrants further investigation, particularly with other chemo-immunotherapeutics or cancer vaccines as a promising combinatorial therapeutic approach for localized treatment of GBM.

Riassunto

Il glioblastoma, un glioma di grado 4, è il tumore cerebrale maligno primario più comune negli adulti. E' una malattia senza cura, con una sopravvivenza media di 14-16 mesi. Il protocollo di cura è rimasto pressoché invariato dal 2005 (protocollo di Stupp), e consiste nella resezione chirurgica della massa tumorale seguita da radioterapia e chemioterapia sistemica con temozolomide (TMZ) combinata con corticosteroidi.

La resistenza alle terapie attuali è dovuta a diversi fattori, tra cui la barriera ematoencefalica, che ostacola il passaggio e la distribuzione dei farmaci dopo somministrazione sistemica, l'elevata eterogeneità intra- e intertumorale del GBM tra i pazienti e la capacità del tumore di sviluppare resistenza ai farmaci.

Questo studio propone lo sviluppo di un sistema di drug delivery locale polimerico in grado di penetrare nel tumore, per veicolare localmente il farmaco antitumorale paclitaxel (PTX). Il nuovo nanocarrier e' composti da Acido Ialuronico (HA) e Poli-L-Lisina (PLL). L'HA (100 kDa) e' stato selezionato, grazie alla sua somiglianza con la matrice extracellulare (ECM), offre sicurezza e biodegradabilità, mentre la sua variante a basso peso molecolare mostra potenziale per la modulazione immunitaria tramite interazione con le cellule del GBM e del sistema immunitario. La PLL (8.2 kDa), grazie alle sue cariche positive, facilita l'internalizzazione all'interno della complessa architettura del GBM.
Le nanoparticelle sono state assemblate utilizzando un sistema basato su microfluidica, attraverso l'interazione tra le cariche opposte di HA e PLL. Inoltre, i due polimeri sono coniugati con linker bioortogonali, garantendo la stabilità delle nanoparticelle in ambiente fisiologico. Le nanoparticelle sono state analizzate chimico-fisicamente utilizzando ^{1}H-NMR, Dynamic Light Scattering e TEM, tra le altre tecniche, per ottenere una caratterizzazione completa.
Studi preliminari in vitro sulle nuove nanoparticelle sono stati condotti su cellule murine SB28 di GBM.

Infine, dopo aver determinato l'IC_{50} su SB28, il PTX è stato coniugato alle nanoparticelle tramite un linker bioresponsivo e la nuova nanomedicina è stata completamente caratterizzata usnado metodi chimico-fisici. Il potenziale terapeutico di questa nuova nanopiattaforma merita ulteriori studi in vitro e in vivo in particolare al fine di sviluppare nuovi approcci combinatoriali per il trattamento chemo-immunoterapico del GBM.

1. Introduction

1.1. Glioblastoma

Glioma (GLM) is a prevalent type of tumor that originates in the brain[1]. This tumor arises from glial cells, which are the supportive cells within the brain and spinal cord. A distinction is made between primary and secondary cancers: primary tumors develop at the site of origin, while secondary tumors result from the spread of cells from a different location[1].

The World Health Organization (WHO) has established an international standard for the classification and diagnosis of GLMs. This classification system ranks GLMs from grade 1 to grade 4 based on the level of malignancy, as determined by histopathological criteria[1]. Grade 1 GLMs exhibit low proliferation potential and can typically be treated effectively through surgical procedures. Conversely, GLMs of grades 2 to 4 are progressively more malignant and invasive.

Glioblastoma (GBM), also known as Glioblastoma Multiforme, is a grade 4 GLM that originates from degenerating astrocytes. It is the most frequent primary malignant brain tumor, representing 80% of such cases[2]. GBMs typically arise in the brain's lobes, with the frontal and temporal lobes being the most affected[3]. GBM exists in two forms: primary and secondary. The primary type (also known as *de novo*) is the most prevalent, representing 90% of all GBM cases. Secondary GBM, in contrast, accounts for approximately 10% of cases [4]. The primary form is highly aggressive, with a growth rate of 1.4% per day and a doubling time between two weeks and 49.6 days[5]. This type commonly affects older adults, with an average onset age of 62 years[6]. Secondary GBM is generally less aggressive, progresses at a slower rate, and predominantly affects younger patients, with a mean age of 45 years[6]. This type often arises from lower-grade GLMs that have advanced into GBM[7]. Despite its relatively low incidence of 3-5 cases per 100,000 people globally, GBM leads to approximately 200,000 deaths each year[8]. The median survival time for GBM patients is 14-17 months, indicating the challenging nature of its treatment and the urgent need for new therapeutic strategies[9]. Only 5% of patients survive beyond five years post-diagnosis.

1.2. Glioblastoma treatment

The effective treatment of GBM is significantly hindered by the inability to target all tumor cells comprehensively. Surgical intervention, while a cornerstone of initial treatment, is often insufficient due to the diffuse and infiltrative nature of the tumor, which precludes complete

resection without compromising healthy brain tissue. The extent of tumor resection has been shown to influence prognosis in newly diagnosed patients. However, certain anatomical locations, such as the cortex, basal ganglia and brainstem, pose significant surgical challenges, making complete resection unfeasible and leading to a poorer prognosis in affected individuals[10].

Chemotherapy also faces substantial obstacles in the treatment of GBM. A major limitation is the Blood Brain Barrier (BBB), which restricts the penetration of many chemotherapeutic agents into the brain parenchyma, thereby impairing drug delivery to the tumor. Even the most effective agents in glioma therapy achieve suboptimal concentrations in the peritumoral tissues. Additionally, patients with Central Nervous System (CNS) tumors frequently require concomitant treatments, such as corticosteroids, which can further reduce the efficacy of chemotherapeutics and exacerbate adverse effects[10].

Another significant barrier to effective GBM treatment is the tumor molecular complexity and heterogeneity. This intrinsic variability renders a standardized therapeutic approach ineffective, it is really difficult to find a strategy that fits all different types and the standard strategy fails to address the diverse biological characteristics of the tumor in individual patients. These limitations collectively underscore the critical need for innovative and targeted therapeutic strategies tailored to overcome the challenges posed by GBM unique biology and treatment barriers[10].

The standard of care of Glioblastoma: The Stupp protocol

The current standard of care (SOC) for newly diagnosed GBM, widely known as the Stupp protocol, has remained largely unchanged since its introduction in 2005. This treatment approach begins with maximal safe surgical resection of the tumor, followed by six weeks of localized radiotherapy (typically delivering a total dose of 60 Gy) in combination with systemic chemotherapy using the alkylating agent temozolomide (TMZ) (75 mg/m² daily). Subsequently, patients undergo a minimum of six months of adjuvant TMZ treatment, administered at 150–200 mg/m² for five consecutive days in every 28-day cycle[11].

Despite its widespread implementation, the Stupp protocol does not account for the molecular heterogeneity of GBM. Temozolomide is an alkylating agent used as chemotherapy for GBM.

TMZ can alkylate or methylate DNA, usually at the O^6 position of guanine residue, creating DNA damage which eventually leads to cell death[12].

A key factor influencing the response to temozolomide therapy is the methylation status of the O^6-methylguanine-DNA methyltransferase (MGMT) promoter. This DNA repair enzyme counteracts TMZ-induced DNA damage by removing methyl groups from the O^6 position of guanine residues, thereby enabling proper DNA replication[13]. Patients with a methylated MGMT promoter exhibit better outcomes, both in terms of prognosis and response to alkylating therapy, compared to those without methylation. Median survival is 21.7 months for patients with a methylated promoter versus 15.3 months for those lacking methylation. However, despite these molecular insights, the SOC remains uniform for most patients, irrespective of their MGMT methylation status.

While the protocol represents a significant advancement in GBM management, its effectiveness is limited by high recurrence rates and the eventual development of resistance to TMZ. Recurrences typically occur near the initial resection site and re-resection is feasible for only 20–30% of patients[14]. Recurrent tumors often acquire additional genetic mutations, further diminishing the efficacy of radiotherapy and chemotherapy. Moreover, the alkylating action of TMZ becomes less effective over time due to MGMT-mediated repair mechanisms.

The SOC is also associated with substantial complications. Surgical interventions may lead to neurological impairments and regional deficits, while systemic administration of TMZ frequently causes side effects such as nausea, fatigue and organ toxicity, all of which significantly reduce the quality of life for patients[15]. Other significant adverse effects associated with TMZ therapy are hematologic complications, including neutropenia, thrombocytopenia, lymphopenia and leukopenia. Although rare, TMZ may also lead to liver damage, making routine monitoring of liver function highly advisable[16]. Furthermore, the adjunctive use of corticosteroids, often required to manage peritumoral edema, can exacerbate these challenges by contributing to additional systemic side effects.

Despite its limitations, the Stupp protocol remains the pillar of GBM treatment. However, the lack of durable responses[17] and minimal progress in therapeutic innovation over the past two decades highlight the pressing need for novel, targeted strategies capable of overcoming the challenges of GBM molecular complexity, recurrence and resistance mechanisms.

1.3. Challenges in GBM treatrments

Figure 1 provides a summary of the key characteristics that contribute to the challenges in treating GBM. These include its anatomical location, which, being protected by the BBB, prevents the majority of systemically administered drugs and molecules from effectively reaching the tumor site. Another critical factor is the substantial intra- and intertumoral heterogeneity of GBM, which complicates the development of a universally effective therapy. Additionally, the tumor is characterized by the presence of a specialized tumor microenvironment, termed the tumor immunosuppressive microenvironment (TIME), which inhibits the body ability to recognize and mount an immune response against the tumor. Lastly, the presence of specific cell types, such as glioblastoma-associated stem cells (GSCs), further contributes to the tumor resistance to conventional therapeutic approaches.

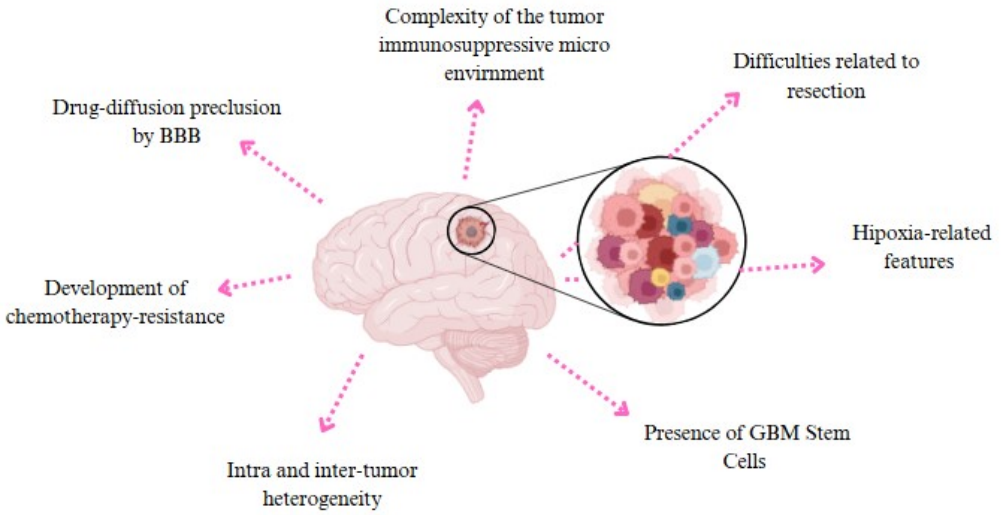

Fig. 1*. GBM features that cause the unresponsiveness to the GBM therapies*

Chemotherapy resistance

The resistance of GBM to therapy, together with its rapid proliferative capacity, is a significant factor underlying the low life expectancy associated with this aggressive cancer. Multiple biological mechanisms contribute to the poor response of GBM to antineoplastic treatments, with the TME playing a particularly crucial role in promoting chemoresistance[18]. The TME, composed of a variety of cells, signaling factors and unique conditions, provides a supportive environment that sustains GBM growth and selectively promotes the most aggressive cancer

cells. This microenvironment influence is especially prominent in GBM due to the tumor intrinsic heterogeneity and ability to exploit various survival pathways.

Another key role is played by GSCs, characterized by their capacity for self-renewal and tumor initiation and they contribute to the aggressive nature of GBM by mediating resistance to both chemotherapy and radiotherapy, enhancing invasion and driving tumor recurrence and metastasis[19]. The TME supports these GSCs, reinforcing their stem-like properties and sustaining processes that fuel therapeutic resistance and tumor progression.

Among the challenges in treating GBM is the tumor frequent resistance to Temozolomide, the standard chemotherapeutic agent included in the Stupp Protocol. This resistance is often exacerbated by GBM high mutation rates and adaptability. Unfortunately, over 50% of GBM patients fail to respond to TMZ[20]. TMZ resistance is made by MGMT by directly repairing the drug-induced DNA alkylation damage. Specifically, MGMT removes the methyl group from O^6-methylguanine, reversing the DNA damage caused by TMZ and thereby decreasing the drug efficacy.

The MGMT gene promoter methylation status is an important predictor of TMZ response. Uunmethylated tumors, associated with increased MGMT activity, tend to be resistant to TMZ. Consequently, the MGMT promoter unmethylation status has been established as a key epigenetic marker of intrinsic TMZ resistance, underscoring its importance in therapeutic decision-making for GBM[21].

The Blood-Brain Barrier

One of the major limitations of GBM therapy is its anatomical location. GBM is located within the brain, one of the most protected organs due to the presence of the BBB and among the most challenging to access through systemic administration of drugs.

The BBB is a highly specialized structure formed by endothelial cells that line the capillary walls within the CNS. The integrity of BBB is maintained through close inductive interactions with various cell types, particularly the end feet of astrocytic glial cells. Supporting cells such as pericytes, microglia and nerve terminals also play crucial roles in inducing, maintaining and modulating BBB function[22].

The role of the BBB is to protect the brain, from the potential toxicity of neurotoxins and macromolecules, while allowing the entry of ions, nutrient molecules and neurotransmitters[23]. Small (< 400 Da) and lipid-soluble (logP > 3) drugs can passively diffuse

across the BBB where the large (> 400 Da) or water-soluble (logP < 3) drugs are stopped by a complex network of tight junctions[24]. This represents a big challenge for the systemic treatment of brain tumors such as GBM, since the amount of drug that can achieve the brain passing through the BBB is really limited. Many brain tumors such as metastasis of lung, breast, melanoma and renal cancers[25], exhibit a disruption in the integrity of the BBB, resulting in an increased possibility of its crossing. This phenomenon also occurs in GBM, due to the alteration of structural proteins responsible for the non-permeability of tight junctions, such as claudin-3 and claudin-5 [26]. While this might appear advantageous from a therapeutic perspective, as it could allow chemotherapeutic agents to reach the tumor site (typically hindered by the BBB), the reality is that this effect is not entirely beneficial. The BBB disruption is not uniform and may remain completely intact in various regions of the GBM. Moreover, barrier disruption can enhance tumorigenicity by permitting the infiltration of pro-tumorigenic cells, such as peripherally-derived immunosuppressive macrophages (referred to as M2-like tumor-associated macrophages, TAMs)[27].

Heterogeneity

One of the critical challenges in the treating of GBM is its related to its heterogeneity. This tumor exhibits both intratumoral heterogeneity, where cells within the same tumor mass can display different phenotypes and characteristics, and intertumoral heterogeneity. Additionally, GBM is marked by significant genetic, clinical, biological, and molecular variability. Understanding these differences and investigating genetic modifications can help predict GBM response to therapies. For instance, resistance to systemic therapy with TMZ is linked to a genetic alteration involving the overexpression of the gene encoding O^6-methylguanine-DNA methyltransferase (MGMT). MGMT is an enzyme capable of repairing the DNA damage caused by TMZ by removing the O^6 group from DNA, thereby allowing normal DNA replication[13]. By identifying potential genetic alterations and correlating them with their phenotypic manifestations, it is possible to predict both the aggressiveness of GBM and its sensitivity to chemotherapy.

GBM encompasses two distinct subtypes, primary and secondary, which differ significantly in their onset, patient demographics and underlying genetic pathways. Primary GBMs, accounting for the majority of cases (>90%), arise rapidly de novo, without any preceding clinical or histopathological evidence of a less malignant precursor lesion. These tumors predominantly affect older adults, with a mean age at diagnosis of 62 years, and exhibit a higher incidence in

men, with a male-to-female ratio of 1.33:1 [28]. In contrast, secondary GBMs emerge through the progression of lower-grade gliomas, such as diffuse astrocytomas or anaplastic astrocytomas, and they are generally less aggressive. These tumors are more commonly diagnosed in younger individuals, with a mean age of 45 years and show a higher prevalence in women, with a male-to-female ratio of 0.65:1. Unlike primary GBMs, secondary glioblastomas result from a stepwise accumulation of genetic alterations over time[29]. This stark contrast in age distribution, gender prevalence and genetic progression between primary and secondary GBMs underscores the heterogeneity of glioblastoma as a disease. From a genetic perspective, it is essential to distinguish between primary and secondary GBM, as they exhibit distinct genetic alterations [30][31][32][8].

EGFR amplification or mutations are common in primary GBMs, such as in other types of aggressive tumors[33]. EGFR protein stimulates the cell division, inducing the cell survival and invasion. EGFR is known to be a driver of the Ras pathway. Also, p53 is known to be mutated in GBM. Protein p53, codified by the TP53 gene, is a transcription factor that regulates cell cycle progression, DNA repair, apoptosis, and senescence in response to cellular stress or DNA damage. The TP53 gene is thought to be mutated or deleted in approximately 50% of human cancers, including GBM[34]. Modification in this gene was correlated with secondary GBM, but recently scientists found TP53 mutations in many primary glioblastomas. However, the p53 protein pathway can also be suppressed through mechanisms other than direct mutation of the TP53 gene. One mechanism is the amplification of the gene encoding the ubiquitin ligase MDM2, a protein that promotes the degradation of p53, thereby inhibiting its signalling. Increased transcription and translation of the gene encoding MDM2 is observed in over 10% of primary GBM [30],[35]. Another important mutation observed in primary GBM is the mutation or suppression of PTEN gene expression. PTEN is a potent inhibitor of the oncogenic Akt pathway. The suppression of this gene induces the hyperactivation of the Akt signaling pathway, a critical regulator of numerous cellular functions, including metabolism, growth, and survival. This dysregulation disrupts the balance of intracellular signaling, leading to uncontrolled cell proliferation, enhanced migratory, invasive potential, and increased angiogenesis, which facilitates tumor vascularization. Additionally, the hyperactivation of Akt contributes to resistance against conventional therapies by promoting cell survival under otherwise lethal conditions. These changes collectively drive the aggressive progression and enhanced survival capabilities of glioblastoma cells [36].

Secondary glioblastomas, however, are also characterized by specific alterations. Among these is the metabolism-related gene isocitrate dehydrogenase 1 (IDH1), which has been founded

mutated in 70% of secondary GBMs examined. Many glioblastomas lacking this mutation were found to harbour a mutation in the IDH2 gene instead [37]. The amplification of the gene encoding for platelet-derived growth factor receptor (PDGFR) is also observed in secondary GBM [38].

In addition to the genetic alterations' characteristics of primary or secondary GBM, there are genetic modifications present in both types of GBM or whose frequency of occurrence is not distinctly associated with one type over the other. Among these is the loss of heterozygosity on chromosome 10q, observed in 80% of primary GBM cases and 70% of secondary GBM cases analyzed[39][40]. As previously mentioned, the p53 protein pathway can also be suppressed through alternative mechanisms that do not directly involve the TP53 gene. In 40-50% of GBM cases, there is an alteration affecting cyclin-dependent kinase inhibitor 2A (CDKN2A), a gene that encodes proteins with various tumor-suppressive functions. Specifically, this gene encodes the protein p14ARF, which downregulates MDM2. Consequently, by suppressing CDKN2A gene expression, there is a reduced expression of the p14ARF protein, leading to increased MDM2 expression and thus silencing of the p53 pathway, which results in enhanced cell division and differentiation [41]. There are also alterations in genes involved in the regulation of kinases that play important roles in the cell cycle. These modifications are observed in all types of GBM, with a frequency of around 14%. Among these are the mutation or silencing of the RB1 gene and the amplification of the CDK4 gene [42]. These are some of the modifications that lead to upregulation of the cell cycle within GBM.

Also, due to the integration of additional genomic and transcriptomic data, the identification of four key molecular subtypes of GBM with significant clinical relevance was done: neural (NL), proneural (PN), mesenchymal (MES), and classical (CL) GBM. The neural subtype shows gene expression patterns similar to those in normal brain tissue and often demonstrates greater responsiveness to radiation and chemotherapy. Invasive biopsy or surgical resection are the mothods to determine a patience tumor subtype[43]. Proneural GBM, typically found as a secondary GBM in young adults, is marked by mutations in the TP53 and IDH1/2 genes. Classical GBM is distinct for its absence of p53 mutations, its chromosomal alterations (such as chromosome 7 amplification or deletions), and elevated EGFR amplification levels. The mesenchymal subtype, predominantly a primary GBM observed in older adults, is promoted by mesenchymal differentiation and characterized by EGFR overexpression, which serves as a crucial marker for mesenchymal GBM proliferation. Among these subtypes, mesenchymal GBM exhibits particularly high invasiveness and infiltration capabilities, allowing it to spread

into the surrounding brain tissue. In addition, a shift from PN to MES subtype can occur in patients following radiation therapy and chemotherapy [44].

Tumor Immunosuppressive MicroEnvironment (TIME)

GBM arises within an immunosuppressive tumor microenvironment (TIME) that fosters both tumor cell proliferation and enhanced malignancy [45]. The progression of tumor growth into cancer fundamentally hinges on the tumor ability to evade and escape immune surveillance mechanisms. This is supported by the TIME, consisting of diverse cell types (resumed in *Figure 2*), including infiltrating tumor cells and cancer stem cells, as well as non-cancerous cells like myeloid cells (resident microglia and bone marrow-derived macrophages), tissue-resident cells (such as neurons and astrocytes) and lymphocytes, all of which interact within this complex network. GBM cells actively release chemokines, growth factors, and cytokines, which attract and stimulate immunosuppressive cells in the TIME. These recruited cells, in turn, engage with GBM cells via various immunosuppressive receptors, facilitating tumor growth, promoting resistance and enabling evasion from immune surveillance [15].

GBM cells demonstrate a loss of Major Histocompatibility Complex (MHC) class II expression, a molecule typically restricted to antigen-presenting cells (APCs) and crucial for antigen cross-presentation to adaptive immune cells. This phenomenon is particularly evident in microglia, highlighting the tumor's extensive immunosuppressive influence [46]. The GBM TIME is characterized by high levels of immunomodulatory factors, including transforming growth factor β (TGF-β), interleukin-10 (IL-10), and prostaglandin E2 (PGE2). Evidence increasingly indicates that these factors, especially TGF-β secreted directly by GBM cells, drive the transition of brain-resident and infiltrating immune cells, such as microglia and tumor-infiltrating myeloid cells, toward an immunosuppressive phenotype. This shift facilitates aggressive tumor growth and progression while simultaneously suppressing anti-tumor immune responses [47].

One of the most extensively studied immunosuppressive receptors involved in immune escape in GBM is Programmed cell death protein (PD)-1 [48]. Expressed primarily on activated T cells, PD-1, when bound to its ligand (PD-L)-1, leads to T cell inactivation. In GBM, PD-L1 is notably overexpressed by both GBM cells and myeloid cells, allowing effective PD-L1/PD-1 binding and subsequent immune response inhibition.

Additional factors derived from GBM, such as interleukin-6 (IL-6), play a significant role in modulating the tumor microenvironment. IL-6 aids in the recruitment of myeloid cells and shifts the immune response away from inflammatory, anti-tumor activity toward anti-inflammatory and wound-healing pathways. This transition reduces the ability of immune cells to effectively target and destroy tumor cells. Furthermore, IL-6 contributes to tissue remodeling, fostering an environment of immune privilege that impedes immunological access to tumor cells, thereby supporting tumor survival and progression [49].

Among non-neoplastic cells in the GBM TME, tumor-associated microglia and macrophages (TAMs) are predominant, making up approximately 30% of the TIME. In a healthy CNS, microglia and macrophages serve as the primary innate immune cells, maintaining homeostasis and overseeing immune functions. The partial disruption of the BBB in GBM allows infiltration by peripheral bone marrow-derived macrophages, which make up about 85% of TAMs in these tumors [50]. TAMs typically display two main phenotypes: the M1-like phenotype, characterized by inflammatory and anti-tumor activity and the M2-like phenotype, which is associated with anti-inflammatory, pro-tumoral functions. High infiltration of M2-like TAMs has been correlated with poor prognosis in GBM. TAMs not only promote tumor proliferation and angiogenesis but also suppress effector T cell proliferation and attract regulatory T cells (Tregs) and myeloid-derived suppressor cells (MDSCs) through cytokine release.

MDSCs represent a heterogeneous population of monocytic cells implicated in tumor-driven immune suppression across various cancers, including GBM [51]. These cells exert their immunosuppressive effects locally by releasing cytokines such as IL-10, TGF-β, inhibiting conventional T cells and upregulating immunosuppressive molecules like programmed death-ligand 1 (PD-L1), collectively inhibit the adaptive immune response [52],[53]. The classification of MDSCs continues to evolve, typically involving a combination of surface marker profiles and functional assays, such as their ability to suppress T cell activation and proliferation or their release of immunosuppressive cytokines like IL-10. The principal MDSC subtypes include monocytic MDSCs, (M-MDSCs), polymorphonuclear (PMN-MDSCs) and granulocytic MDSCs (G-MDSCs), alongside other immunosuppressive monocytes such as early MDSCs and non-classical monocytes. MDSCs play a crucial role in maintaining the immunosuppressive microenvironment in glioblastoma. By interacting with various cellular components of the TME, they enhance regulatory Treg functions, suppress antigen presentation and inhibit the activity of effector T cells, thereby facilitating tumor progression [53].

Tregs are highly immunosuppressive and play central roles in maintaining self-tolerance and immune homeostasis; however, in malignant tumors, they promote tumor progression by

suppressing effective antitumor immunity[54]. They further support immunosuppression within the TIME by inhibiting effector T cells and antigen-presenting cells (APCs). GBM tumors typically exhibit a low density of tumor-infiltrating lymphocytes (TILs) and a limited presence of infiltrating natural killer (NK) and B cells. Additionally, GBM tumors produce relatively low levels of tumor-associated antigens, which may limit the effectiveness of immunotherapeutic approaches.

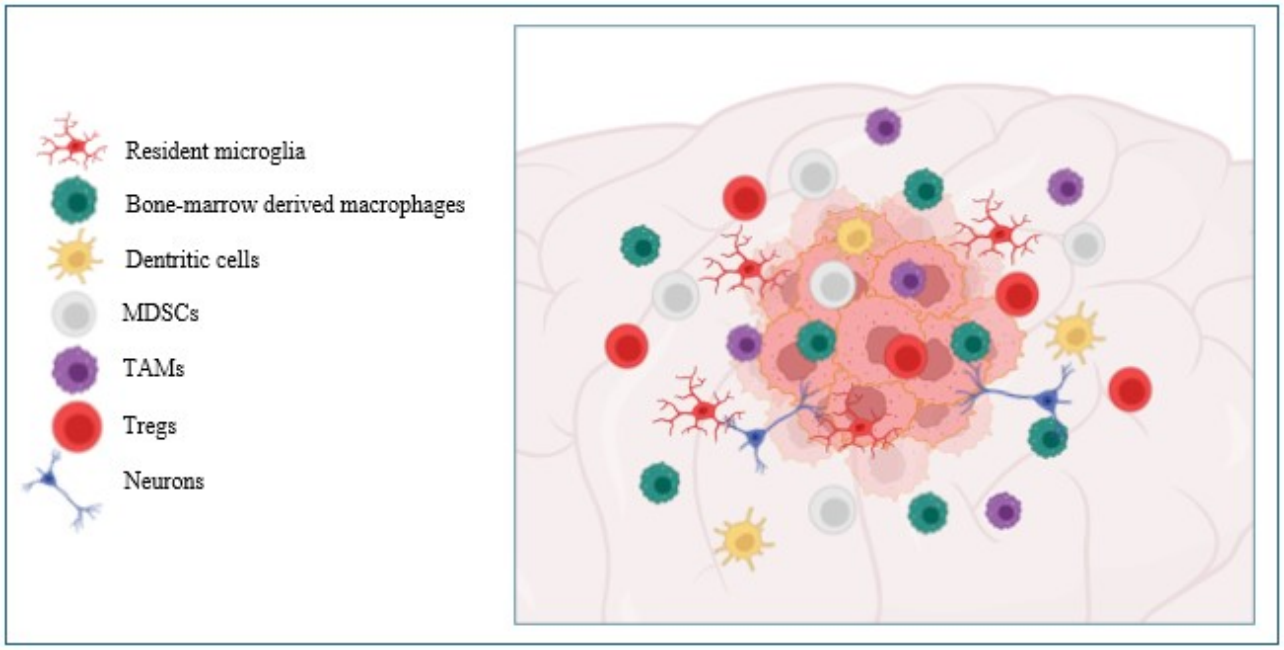

***Figure 2**: Representation of tumor immunosuppressive microenvironment and associated cells. (Abbreviations: MDSC = Myeloid-derived suppressor cells, TAMs = tumor-associated microglia, Treg = regulatory T cells)*

Glioblastoma Stem Cells

Glioblastoma stem cells (GSCs) represent a distinct and functionally unique cell population within GBM. These cells are characterized by their transcriptional, epigenetic and metabolic regulatory differences compared to more differentiated tumor progeny, highlighting the complexity of targeting them therapeutically [55]. GSCs are central to the resistance mechanisms observed in GBM, including radioresistance, chemoresistance, angiogenesis, invasion and recurrence. Their ability to resist therapy is partly due to their high metabolic demands, which drive both rapid proliferation and the maintenance of their stem-like properties.

Metabolic reprogramming plays a crucial role in the survival and aggressive behavior of GSCs [56]. The metabolism of GSCs is highly plastic, with fast-dividing cells relying on anaerobic glycolysis, thus creating the Warburg effect, a metabolic adaptation that supports rapid tumor growth. In an acidic environment, GSCs can undergo mesenchymal differentiation, further increasing their resistance to therapy. Conversely, slowly proliferating cells tend to rely more

on oxidative phosphorylation and lipid oxidation, making it difficult to target their metabolism pharmacologically [57]. GSCs can adapt to nutrient and stress conditions by modulating their glycolytic activity. Research has shown that GSCs upregulate high-affinity nutrient transporters, such as GLUT3, through dysregulated integrin signaling networks [58]. This allows them to secure glucose, which is essential for fueling the metabolic processes required for cell growth and division. The glucose is then channelled into nucleotide biosynthesis, directly supporting GSC proliferation. Moreover, in the poorly vascularized and necrotic regions of the tumor, GSCs express SHMT2, an enzyme involved in serine metabolism, which helps restrict oxygen consumption, promoting survival under hypoxic conditions [55]. This metabolic plasticity enables GSCs to adapt to the challenging tumor microenvironment, characterized by limited oxygen, nutrients and abundant waste products.

GSCs also interact with immune cells within the tumor microenvironment supporting the immunosuppression, using their metabolism to generate stress that can suppress immune cell activity. By secreting immunosuppressive factors such as IL-10 and TGF-β, GSCs promote an M2-like immunosuppressive phenotype in tumor-associated microglia [59]. Furthermore, GSCs regulate immune responses by activating regulatory T cells, inhibiting cytotoxic T cell proliferation and inducing cytotoxic T cell apoptosis. These interactions contribute to the immune escape mechanisms that allow GBM to evade immune surveillance and continue progressing [60].

Additionally, GSCs exploit several mechanisms to resist therapies. They express drug efflux pumps, such as ABC transporters, to protect themselves from chemotherapeutic agents [61]. Autophagy, which is vital for maintaining stemness in both normal and tumor tissues, has been shown to contribute significantly to therapy resistance in GSCs [62].

Hypoxia

The hypoxic state, which fosters a hypoxic and acidic environment, is another factor contributing to the aggressiveness and invasiveness of GBM. This condition arises due to the formation of discontinuous tumor capillaries, which fail to supply the tumor mass with adequate oxygen and nutrients [63]. This, along with other factors, such as genetic alterations that lead to the overexpression of genes like EGFR, the silencing of the p53 protein pathway (caused by PTEN gene suppression, MDM2 gene overexpression, and CDKN2A gene suppression), and the improper formation of tumor capillaries resulting in thrombotic events and a lack of nutrients and oxygen, triggers the activation of specific transcription factors, such as HIF (an

important regulator of the hypoxic adaptive response). This transcription factor regulates thousands of genes involved in tumor aggressiveness and invasiveness; indeed, the genes under its control are implicated in cell division, migration, promotion of angiogenesis, and cell survival. Hypoxia-mediated invasiveness, the high proliferative capacity of GBM cells, and extensive infiltration are considered the primary factors contributing to chemoresistance and patient mortality in GBM [64]. It is precisely due to the significant proliferative and invasive capacity of GBM cells under hypoxic conditions that complete surgical resection of the tumor is challenging. Frequently, highly infiltrative cells extend deep into healthy brain parenchyma, with the potential to give rise to new tumor masses.

Resection-associated difficulties

The Stupp protocol involves an initial tumor resection. However, with this approach, it is extremely challenging to completely eradicate the tumor mass, as GBM has a high infiltrative capacity and poorly defined margins, resulting in secondary masses or tumor cells deeply embedded within the healthy brain parenchyma [65]. Studies show that at the time of diagnosis, GBM typically invades multiple lobes and both brain hemispheres [66], illustrating its substantial infiltrative potential. Concern over possible damage to essential brain structures and the correlated impairment of the patient's quality of life, often makes achieving total tumor resection challenging or impossible. This limitation allows tumor cells to persist at the resection site, leading to recurrences that can only be reoperated in 20-30% of patients [14].

1.4. Local treatments of Glioblastoma

Systemic therapy for glioblastoma (GBM) remains highly challenging due to multiple inherent limitations. The presence of the BBB is a major obstacle, as it significantly restricts the penetration of therapeutic agents into the brain, resulting in subtherapeutic drug concentrations at the tumor site. Furthermore, systemic administration is often associated with off-target toxicity, limiting the use of high drug doses. This not only reduces the effectiveness of treatment but also contributes to the emergence of drug resistance, which further complicates disease management and reduces patient survival outcomes. Given these limitations, the development of innovative therapeutic strategies for GBM has become imperative. A promising approach involves shifting from systemic therapies to local drug delivery strategies. Localized treatments offer several key advantages: they bypass the BBB, allowing for the direct administration of therapeutic agents to the tumor site at concentrations high enough to exert a robust anti-tumor

effect, while simultaneously minimizing systemic exposure and the associated side effects. Moreover, the unique isolation of the brain due to the BBB creates an opportunity to deliver potent, localized treatments with a reduced risk of systemic toxicity, enhancing both safety and efficacy [67].

Local drug delivery technologies currently under investigation include implantable devices, biodegradable wafers and advanced nanoparticle systems capable of sustained and targeted drug release. These approaches are designed to address the limitations of systemic therapy, offering improved therapeutic outcomes while preserving the quality of life for patients [68]. Local drug delivery has the potential not only to enhance treatment efficacy but also to mitigate the burden of systemic side effects, thereby representing a paradigm shift in the management of GBM.

1.4.1. Direct injection into GBM

To overcome the limitations posed by the BBB and increase therapeutic concentrations within the brain, direct drug administration into the central nervous system has emerged as a promising approach. This can be achieved through direct injections into the tumor using repeated needle-based injections or catheter implants connected to a reservoir. This method reduces systemic toxicity, allows repeated administrations and enables the infusion of larger drug volumes directly at the target site. However, these techniques can be hindered by potential catheter obstructions, local adverse effects (such as infections and intracranial haemorrhages) and the reliance on passive diffusion for drug dispersion. Since diffusion is limited by the concentration gradient and the compound's diffusivity within the tissue, drug penetration depth is often restricted by the drug's physicochemical properties or by its rapid metabolism [69].

1.4.2. Convection-enhanced delivery

Convection-enhanced delivery (CED) offers an effective strategy to improve drug distribution within the brain. CED utilizes microcatheters, stereotactically implanted and connected to an infusion pump that generates a pressure gradient, enabling uniform drug distribution across a radius of 2–3 cm [70]. The pump generates the pressure to infuse therapeutic drugs at a rate from about 5 µL/min to 10 µL/min. This technique is beneficial also for patients with non-operable or recurrent glioblastomas, as it permits the delivery of high concentrations over larger

volumes with minimal systemic exposure. Unlike passive diffusion, CED enables a more controlled spatial distribution of the therapeutic agent based on where the catheter is located, independent of its molecular weight or diffusivity, and maintains positive pressure for extended periods. The primary limitation of this technique was the inadequacy of early catheter technology, as the initial catheters were susceptible to backflow [71]. Researchers are now focusing on the development of smaller, advanced catheters and innovative systems such as cannula-based approaches, which have helped reduce the side effects associated with CED therapies. Clinical trials exploring CED were first conducted in the early 1990s, utilizing several agents, including standard chemotherapy drugs. Phases I through III of these trials successfully demonstrated that multiple convection-delivered agents exhibited satisfactory safety profiles [71]. Despite this, CED therapy remains unapproved by the FDA for treating GBM patients [72].

1.4.3. Gliadel®

The Gliadel® wafer represents a pivotal advancement in local drug delivery for glioblastoma treatment, specifically designed to circumvent challenges associated with systemic chemotherapy. This biodegradable implant, composed of a 20:80 ratio of 1,3-bis-(p-carboxyphenoxy)propane (PCPP) and sebacic acid (SA), contains 3.85% carmustine (BCNU), a highly lipophilic nitrosourea with a strong ability to penetrate the blood-brain barrier [73]. Once implanted into the tumor resection cavity during surgery, the wafer releases BCNU in a controlled manner, achieving a localized cytotoxic concentration directly within the tumor site while minimizing systemic exposure. BCNU functions primarily by alkylating nucleoproteins, leading to DNA crosslinking, DNA-protein binding, and inhibition of cellular repair mechanisms, those that are especially advantageous given the immune-evasive properties of GBM [74]. The recommended dose of BCNU is 61.6 mg, represented by 8 wafers (7.7 mg BCNU each) that are implanted intracranially to fill the resection cavity. The integration of the drug in the PCPP-SA wafer, protects the BCNU from degradation, releasing it over time and allowing to achieve a high concentration of the chemotherapeutic agent in the resection cavity. Importantly, in vivo studies show that Gliadel® wafers maintain BCNU release over approximately 21 days, with peak release occurring within the first week and complete degradation of the polymer in 6 to 8 weeks. Clinical trials have demonstrated that Gliadel® treatment is associated with increased overall survival (OS) in patients with glioblastoma compared to placebo, though some local side effects, such as seizures, intracranial

hypertension, meningitis, cerebral edema, impaired neurosurgical wound healing and wafer migration [75].

While Gliadel® represents an effective localized treatment strategy, it also reveals limitations: rapid drug release, limited diffusion within tumor margins, single-agent therapy and some side effects. For those reasons, its clinical use is not approved in Europe yet. Given that, not all glioblastoma patients respond effectively to BCNU and the incidence of recurrence remains high. For these reasons, there is an ongoing effort to enhance local delivery systems that can be used for the local treatment of GBM.

1.4.4. Tumor treating fields - Optune®

Tumor Treating Fields (TTF) are alternating electrical fields. The application of those electric fields in cancer therapy has gained significant attention for its potential to inhibit tumor growth effectively. In 2004, Kirson and colleagues demonstrated that intermediate frequency (100–300 kHz), and low-intensity electric fields (<2 V/cm) could reduce tumor cell replication both in vitro in cell cultures and in vivo using mouse models [76]. Studies on pancreatic tumors treated with Tumor Treating Fields showed disruptions in the mitotic cycle, with cells displaying alterations in cytoskeletal components critical for osmotic stability. Notably, treated pancreatic cancer cells exhibited reduced clonogenicity, indicating that TTF therapy could impair cancer cell proliferation [77].

These promising preclinical results paved the way for clinical trials evaluating TTF therapy in patients with recurrent GBM. Despite a challenging patient population with considerable heterogeneity (many experiencing multiple relapses and chemotherapy-resistant disease) TTF therapy achieved encouraging outcomes. Patients receiving TTF therapy experienced a median survival of 6.6 months compared to 6.0 months for those in the control group undergoing chemotherapy ($p=0.27$), with progression-free survival of 2.2 months versus 2.1 months in controls ($p=0.13$) [78]. Importantly, TTF therapy was associated with minimal side effects, predominantly limited to mild skin irritation from the transducer pads.

In recognition of its safety and efficacy, the FDA approved only one TTF devices; in fact, Optune® received regulatory approval for the treatment of supratentorial GBM in adults aged 22 or over for recurrent or refractory GBM [79]. By 2015, the FDA expanded this approval to include adjuvant treatment in newly diagnosed GBM patients following standard-of-care surgery and chemoradiation. The National Comprehensive Cancer Network (NCCN) has since

incorporated TTF as a treatment option for newly diagnosed GBM, supporting its role in modern GBM management.

1.4.5. Virotherapy

Among the emerging treatments for GBM, immunotherapy is one of the most extensively studied. GBM's low immunogenicity, together with its immunosuppressive microenvironment, allows it to escape immune responses. Consequently, numerous local therapies have been developed to enhance the immune system's response, aiming to direct it against glioblastoma. A specific local approach showing potential in clinical trials is viral therapy. Viral therapy can be employed in multiple ways to target GBM. In gene therapy, replication-defective viruses serve as carriers for therapeutic genes, enabling infected cancer cells to produce therapeutic agents [80]. On the other hand, oncolytic viruses, which are often replication-competent, are designed to induce cytotoxic effects specifically within tumor cells. Both strategies aim to activate immune responses and promote antitumor immunity [67]. Numerous viral therapies for glioblastoma have been studied in clinical trials phase I and II[81].

1.4.6. CAR-T cells

Cytotoxic T lymphocytes collected from a patient can be genetically engineered to express chimeric antigen receptors (CARs) designed to recognize specific tumor-associated antigens (TAs). Once reintroduced into the patient, these modified CAR-T cells can selectively target and eliminate cancer cells [82]. CAR-T cell therapies have shown remarkable clinical efficacy in treating hematologic malignancies, inspiring considerable interest in applying this approach to solid tumors, including GBM. However, the effectiveness of CAR-T cells against solid tumors has been limited due to various obstacles, particularly in the case of GBM. Among these are the tumor acquired resistance mechanisms, restricted penetration of therapeutic agents across the BBB, and the immunosuppressive nature of the tumor microenvironment. CAR-T cells also encounter challenges such as inadequate infiltration into the tumor site, limited persistence and insufficient activity once inside the TME, which further hampers their efficacy [83]. Despite these challenges, CAR-T cell therapy presents a promising strategy to address the shortcomings of the immune system and overcome the barriers imposed by the BBB and the TIME in GBM. The identification of highly specific antigens expressed on glioblastoma cells has been a critical step in advancing CAR-T cell therapies. Additionally, recent insights into the

human glioma TIME have clarified the immunosuppressive and immune-evasive mechanisms that limit CAR-T cell effectiveness, guiding efforts to improve therapeutic outcomes. Various glioblastoma-specific cell surface antigens have been identified as potential targets, including epidermal growth factor receptor variant III (EGFRvIII), HER2, interleukin-13 receptor alpha-2 (IL13Rα2), B7-H3 and disialoganglioside GD2 [83]. These antigens have undergone investigation in preclinical animal models and clinical trials, underscoring their potential in treating GBM. Current research is focused on optimizing CAR-T cell constructs and exploring innovative delivery strategies to enhance their ability to overcome GBM unique barriers, providing a foundation for future improvements in solid tumor immunotherapy.

1.5. Nanomedicines

Nanomedicine, an emerging field within nanotechnology, focuses on the application of nanoscale materials and systems for therapeutic and diagnostic purposes. Defined as the intentional design, characterization, production and application of materials and devices with dimensions between 10 and 100 nanometres, nanotechnology enables the manipulation of structures at a molecular scale [84]. This unique scale allows for the development of particles and devices that can mimic or interact with biological molecules, making them highly suitable for medical use. Nanomaterials can be tailored in size, shape, chemical composition, surface properties and structural characteristics, which allows for the creation of sophisticated drug delivery systems, imaging contrast agents and diagnostic tools [85]. These properties are leveraged in the design of advanced therapeutic agents capable of delivering drugs directly to target cells, improving treatment efficacy and reducing systemic side effects. Many nanomedicines are in clinical trials or have been approved by regulatory bodies FDA, signaling their growing relevance in modern medicine. Nanomedicine thus represents a frontier in personalized medicine, offering promising solutions for complex diseases, including cancer, by providing targeted, efficient and minimally invasive treatment options.

Nanomedicines are characterized by unique properties that may prove valuable in the challenging treatment of GBM. Another significant feature of nanomedicines is their ability to enhance drug stability by encapsulating the active substance, thus protecting it from potential degradation in the physiological environment, such as enzymatic activity. They also improve solubility and pharmacokinetics by providing a controlled release over time, which reduces toxicities associated with side effects. Furthermore, nanoparticles smaller than 100 nm can diffuse through the brain parenchyma, releasing the drug and targeting even deeply located

GBM cells. For instance, a polymeric nanoparticle can encapsulate multiple chemotherapeutic agents, even of different types, allowing for the delivery of a combination therapy. This capability is particularly useful in glioblastoma therapy, where monotherapy frequently leads to resistance, rendering it ineffective. An additional advantage of this technology is its potential for specific targeting, achievable either through the natural tropism of the molecules used or by decorating a targeting molecule to the nanocarrier to enable active targeting. The compounds used in formulating these nanocompounds are also biocompatible, biodegradable and non-toxic, aligning with the safety requirements of biomedical applications.

For these reasons, nanomedicine seems to be promising in the treatment of GBM. Several types of nanomedicines have been exploited for the treatment of GBM including liposomes [86], polymer nanoparticles [87], lipid nanocapsules (LNCs) [88, 89], polymers mixtures and hydrogels [90], metallic nanoparticles[91], dendrimers[92] and microspheres [93]. Active molecules anti-GBM can be loaded or conjugated into those nanocarriers [94].

1.5.1. Polymer therapeutics

"Polymer therapeutics" is a term used to describe a group of polymer-based constructs that includes polymeric drugs, polymer conjugates with proteins, drugs or aptamers, and systems such as block copolymer micelles and non-viral vectors containing covalent linkages [95]. These advanced constructs, classified as "drugs" or "macromolecular prodrugs," differ from conventional drug delivery systems that rely on the non-covalent entrapment of therapeutic agents. Critical attributes of polymer therapeutics include molecular weight, polydispersity, size, structural architecture, and surface properties, such as hydrophilicity, hydrophobicity, and charge density [95]. Since their inception in the 1960s, polymer therapeutics have advanced significantly, with synthetic polymer drugs, polymer-drug conjugates and PEG-protein conjugates emerging as pivotal innovations. The first polymer-drug conjugate to reach Phase I/II clinical trials was the HPMA-doxorubicin conjugate [96]. Subsequent developments led to the commercialization of various polymer therapeutics, including polymeric sequestrants [97], PEG-protein conjugates [98], and the PEG-aptamer conjugate Macugen [99]. Notable examples include PEGylated interferons (Pegasys, Peg-Intron) and PEGylated rhG-CSF (Neulasta), which serve as critical components in cancer chemotherapy [100]. In the 1980s, dendrimers were introduced as a promising class of polymers due to their potential for superior compositional control, three-dimensional architecture, and multifunctionality [101]. However, their clinical translation has proven challenging. Conversely, polyglutamic acid (PGA) has

emerged as an effective drug carrier, with several PGA-based anticancer conjugates undergoing clinical trials. Among these, PGA-Ptx (OPAXIO™) advanced to Phase III trials for GBM therapy. While hematologic toxicity was identified, the combination of OPAXIO™ with TMZ and radiotherapy demonstrated improved progression-free and overall survival rates, highlighting its potential to enhance GBM treatment outcomes [102]. Despite the promising applications of parenteral conjugates such as PEG and HPMA copolymers, concerns about bioaccumulation persist. Although their molecular weight can be optimized for renal elimination, these polymers are non-biodegradable, posing risks of intracellular accumulation and lysosomal storage diseases when administered repeatedly or in high doses [103]. This limitation is particularly concerning for chronic parenteral therapies [104]. To mitigate these issues, biodegradable polymers have gained traction as alternatives for developing protein- and drug-conjugates. Examples of biodegradable polymers undergoing clinical exploration include PGA (degraded by lysosomal cathepsin B), dextrin (degraded by α-amylase), hydroxyethyl starch (HES), "Fleximer" polyacetal technology, poly(sialic acid) and hyaluronic acid (degraded by hyaluronidase) [105].

1.5.2. Polymeric nanocarriers for the treatment of the GBM

Recently, polymeric biomaterials have emerged as promising candidates for nanocarriers in drug delivery systems, particularly for GBM treatment. These materials enable the development of biocompatible systems capable of delivering drugs in a site-specific and time-controlled manner, minimizing neurotoxicity. Furthermore, such systems can serve a dual role as scaffolds and delivery platforms, interacting with GBM cells, healthy brain tissue and the tumor microenvironment [106]. Following the success of the Gliadel wafer, pCPP wafers have been integrated with various chemotherapeutics and tested in animal models, showing safe and effective intracranial delivery[107]. Studies using pCPP wafers loaded with TMZ in rat models demonstrated significant improvements in survival rates. For instance, rats treated with two 50% TMZ wafers exhibited a median survival of 92 days, outperforming the control group and those receiving oral TMZ only (13 and 22.5 days, respectively) [108]. Polymers such as poly(lactic acid) (PLA), poly(ε-caprolactone) (PCL), poly(butyl-cyanoacrylate) (PBCA), poly(glycolic acid) (PGA), PLGA, and poly(amino acids) are commonly used in the fabrication of nanoparticles [109]. Among these, PLGA, PLA, PGA and HA are preferred for brain drug delivery due to their high biocompatibility and low toxicity.

Polymer nanoparticles (PNPs) offer several advantages, including enhanced release profiles, improved compatibility with active agents, resistance to oxidation and longer shelf-life. Additionally, surface modifications can enable PNPs to actively target tumor-specific molecules, increasing drug uptake in GBM cells [110]. Active targeting strategies exploit receptors like transferrin and low-density lipoprotein receptor-related protein (LRP), both overexpressed in GBM cells. PNPs coated with Angiopep or anti-transferrin can cross the BBB and specifically target GBM cells [111]. Preclinical studies on GBM-bearing rats demonstrated that locally administered PTX-loaded PLGA-co-PEG nanoparticles delayed tumor progression and enhanced anticancer efficacy compared to standard PLGA-PTX NPs[112]. Similarly, a study on mice models revealed that injecting PTX-loaded PLGA nanoparticles and TMZ-loaded hydrogels into resection cavities significantly extended median survival times (90, 75, and 37 days for PTX-NPs, TMZ-hydrogel, and resection alone, respectively). Combined therapy showed even greater efficacy, with only 2 out of 9 mice experiencing recurrence within 110 days [113]. Microspheres represent another polymer-based option for GBM treatment. For instance, PLGA microspheres encapsulating 5-fluorouracil, used alongside radiotherapy, showed promise in phase I and II clinical trials, although they failed to improve overall survival significantly [93]. Despite their potential, most polymer-based systems have yet to surpass clinical trials, with Gliadel being the sole exception. These findings underline the necessity of developing new, more effective polymer-based platforms to address the limitations of existing GBM therapies.

Hyaluronic Acid

Hyaluronic acid (HA, 100 kDa) is a polymer that has attracted considerable interest in the design of new drug delivery sistems. It is a linear polymer, specifically a mucopolysaccharide, composed of alternating and repetitive units of N-acetylglucosamine and glucuronic disaccharide (*Figure 3*). Due to its properties such as biocompatibility, non-toxicity, cytocompatibility and remarkable water-binding capacity, it has become a highly investigated polymer in the development of HA-based nanomaterials for various biomedical applications, such as drug delivery systems. Many cells produce HA, and it is one of the main components of the extracellular matrix (ECM) [114].

CD44 is a ubiquitous protein throughout the body with a natural affinity for HA and acts as a receptor, enabling the binding of HA molecules and allowing them to enter the cell via endocytosis. Notably, CD44 has been observed to be overexpressed in many cancer cells,

including those in glioblastoma (GBM). This feature can therefore be exploited in the design of new therapies targeting GBM, utilizing HA as a targeting molecule [115-118].

HA possesses hydroxyl and carboxylic groups, as well as an N-acetyl group, which can be utilized for further chemical modifications. This has enabled the conjugation of various chemotherapeutic agents to HA, with the goal of achieving targeted delivery to cancer cells overexpressing the hyaluronic acid receptor, CD44. Beyond this targeting ability, drug-conjugated HA offers several advantages, including extended circulation time, enhanced drug stability and solubility and improved cancer-targeting efficiency. Once internalized, the HA-drug conjugate is hydrolyzed by intracellular enzymes, facilitating drug release directly to the target cell.

Poly-L-Lysine

Poly-L-lysine (PLL) is a polycationic polypeptide made of a chain of the essential amino acid L-lysine in its alpha form (*Figure 3*). It is extensively employed in drug and gene delivery systems due to its polycationic structure. This polymer is particularly advantageous for biomedical applications, offering attributes such as edibility, water solubility, biodegradability, biocompatibility, and ease of functionalization, with applications spanning from biological adhesives to anticancer agents.

PLL is also categorized within a group of molecules known as "Cell-Penetrating Enhancers" (CPEs), which utilize various pathways to enter cells, including direct membrane entry, endocytosis, and translocation via transient structure formations [119]. So, due to its positive charge, PLL enhances cellular internalization and facilitates the crossing of physiological barriers, including the skin, mucus, and blood-brain barrier, for a wide range of molecules, from nanosized particles to small chemical compounds. Despite its many beneficial properties, PLL can exhibit moderate to high cytotoxicity under physiological conditions due to its cationic nature[120], which may disrupt cellular membranes and induce apoptosis in tumor cell lines.

PLL, being a polycationic polymer, can spontaneously aggregate with polyanionic polymers such as HA, forming nanoparticles through charge interactions.

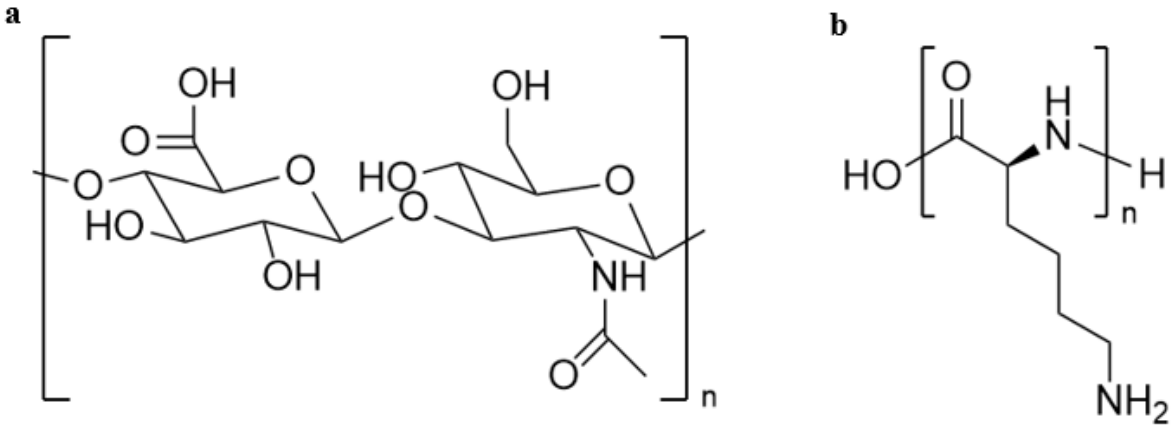

Figure 3. *Chemical structure of Hyaluronic Acid (a) and Poly-L-lysine (b)*

2. Aim of the project

Glioblastoma (GBM) represents a significant unmet clinical need and, despite advances in research, we are still far from achieving a therapeutic solution. The difficulties in identifying an effective therapy stem from the distinct characteristics of GBM, including its high inter- and intra-tumoral heterogeneity, rapid proliferative rate, aggressive infiltration, and challenging anatomical location. GBM develops in the brain, an essential and highly protected organ, safeguarded by the Blood Brain Barrier (BBB) [121]. As the BBB restricts the entry of therapeutics into the brain, high doses of drugs would theoretically be required to reach effective drug concentrations at the tumor site with consequent off-target toxicity. For these reasons, research is increasingly focused on the development of drug delivery systems designed for localized glioblastoma treatment, moving away from systemic administration and its associated disadvantages.

The purpose of this project is to design polymer-based nanoparticles (NPs) as a drug delivery system for the local administration of cytotoxic drugs to GBM. The therapies explored thus far for the local treatment of GBM have exhibited several critical shortcomings, rendering them only partially effective. One of the major drawbacks of these local therapeutic approaches is their low selectivity and inability to distinguish healthy brain parenchyma cells from GBM cells. This lack of specificity results in significant local toxicity, which limits the safe administration of high drug doses.

In this project, Hyaluronic acid (HA, 100 kDa) and poly-L-Lysine (PLL, 8.2 kDa) polymers were selected to design nanoparticles that facilitate their penetration through the brain parenchyma aiming to overcome the challenges associated with the local delivery of therapeutics. HA is widely studied in preclinical and clinical studies due to its advantageous properties, including biocompatibility, non-toxicity, biodegradability, and similarity and compatibility with the extracellular matrix (ECM). Additionally, HA naturally targets CD44, providing an active targeting to GBM cells, and reducing side effects. By promoting their uptake, their dilution, drainage, and thus their elimination by the cerebrospinal fluid (CSF) are reduced and they also allow for less interaction with the healthy cells of the brain parenchyma. PLL is a polycationic polymer known to enhance cellular penetration and can spontaneously aggregate with anionic HA, creating nanoparticles stabilized by opposite-charge interactions. PLL is also biocompatible and non-toxic to the cells.

The NPs were formulated using a microfluidic device equipped with pumps, a technology that uses controlled flows to mix solutions precisely and continuously. The microfluidic method was chosen for its ability to ensure high reproducibility of results, minimizing variations between different production batches. This approach allows the production of NPs with uniform physicochemical

characteristics and offers remarkable scalability. Following the confirmation of the stability and non-toxicity of the formulated NPs, a strategy was developed to conjugate them with an antimitotic drug, Paclitaxel (PTX). Taking advantage of the high intracellular levels of glutathione in the GBM cells, the PTX-conjugation was carried out using a disulfide bioresponsive linker, specifically designed to release the drug after cell uptake. This targeted release mechanism has been designed to minimize side effects and maximize therapeutic efficacy.

3. Materials and methods

3.1. Materials

Hyaluronic acid (HA) with a molecular weight of 100 kDa were purchased from Contipro (Dolni Dobrouc, Czech Republic); Poly-L-Lysine (PLL) hydrochloride with a molecular weight of 8.2 kDa was purchased from Alamanda Polymers (Huntsville, Alabama, USA) ; Methyltetrazine-benzylamine·HCl (Tz-NH_2) and Trans-Cyclooctene succinimidyl carbonate (TCO-NHS) were purchased from Iris Biotech GmbH (Marktredwitz, Germany) ; Dicyclohexyl carbodiimide (DCC), Mercaptopropionic acid and 4-(Dimethylamino)pyridine (DMAP) were purchased from Sigma-Aldrich (St. Louis, MO, USA); Paclitaxel (PTX) was purchased from DBA (Milan, Italy); boric acid (H_3BO_3), potassium chloride (KCl), sodium chloride (NaCl), 4-(4,6-Dimethoxy,1,3,5-triazin-2-yl)-4-methylmorpholinium chloride (DMTMM·Cl), Aldirithiol, cysteamine hydrochloride were purchased from Sigma-Aldrich (St. Louis, MO, USA); Ethanol (EtOH), Methanol (MeOH), Dimetilsulfoxyde (DMSO), Tetrahydrofuran (THF), Diethylether (Et_2OH), Dimetilformammide (DMF) and other solvents not listed, were purchased from Sigma-Aldrich (St. Louis, MO, USA) ; Deuterium oxide 99,9% (D2O), Dimetilsolfoxide-d6 was purchased from Deutero® GmbH (Kastellaun, Germany); Dulbecco's Phosphate Buffered Saline (DPBS), EDTA Bovine Serum Albumin (BSA) were purchased from Gibco (Thermo Fisher Scientific, Waltham, USA); all the salts used for the preparation of Cerebral Spinal Fluid (CSF[122]) and Phosphate Buffered Saline (PBS[123]), were purchased from Sigma-Aldrich (St. Louis, MO, USA). Ultrapure water was used for all the experiments. All other reagents and materials were of the highest analytical quality grade.

3.2.Synthesis of conjugates and derivatives

3.2.1. Synthesis of HA-derivatives building blocks

Hyaluronic Acid-Tetrazine (HA-Tz)

HA (300 mg, 0.744 mmol, 1 eq.) was dissolved in 30 mL of ultrapure water. After HA dissolution, DMTMM·Cl (20.60 mg, 0.07444 mmol, 0.10 eq.) was added to the solution, and the mixture was stirred at RT for 2 h. Next, Methyltetrazine-benzylamine·HCl (14.023 mg, 0.059 mmol, 0.08 eq.) was added to the solution and the mixture was stirred for 72 h at room temperature (RT). Following the time, the reaction was purified by precipitation in ethanol (5 × 200 mL) followed by 24 h of dialysis (membrane cut-off 100 kDa) against water. The final product was then freeze-dried and a pink amorphous solid was obtained. The conjugate has been characterized by ^{1}H NMR and UV–Vis analysis.

Yield: 78% w/w

Pyridyl Disulfide Cysteamine ·HCl salt (PD-NH_2)

Aldrithiol (3304.65 mg, 15 mmol, 1 eq.) was solubilized in 10 mL of MeOH under an N_2 atmosphere. Next, Cysteamine ·HCl (570 mg, 5 mmol, 0.33 eq.) was dissolved in 5 mL of MeOH and then added to the solution. The reaction was allowed to proceed overnight under stirring at RT under an N_2 atmosphere. After that, the product was precipitated in diethyl ether (5 × 200 mL) and then freeze-dried overnight, and a pale yellow solid was obtained. The product was characterized by ^{1}H NMR and Mass Spectrometry analysis.

Yield: 81% w/w

Hyaluronic Acid-Pyridyl Disulfide Cisteamine (HA-PD)

HA (300 mg, 0.744 mmol, 1 eq.) was solubilized in 30 mL of ultrapure water in a round bottom flask with a stirring bar. After the dissolution, DMTMM ·Cl (20.60 mg, 0.07444 mmol, 0.10 eq.) was added to the solution; the mixture was stirred at RT for 3 hours. Next, PD ·HCl (8.43 mg, 0.037 mmol, 0.05 eq.) was added to the solution and the mixture was stirred for 72 hours at RT. Next, the solution was purified by 24 hours of dialysis (membrane cut off 10 kDa) against water. The final product was then freeze-dried obtaining an amorphous white product. The conjugate was then characterized by ^{1}H NMR.

Yield: 95% w/w

Hyaluronic Acid-Pyridyl Disulfide Cisteamine-Tetrazine (HA-PD-Tz)

HA-PD (90 mg, 0.157 mmol, 1 eq.) was dissolved in 30 mL of ultrapure water. Next, DMTMM·Cl (5.21 mg, 0.0188 mmol, 0.12 eq.) was added to the solution and the mixture was stirred at RT for 3 hours. Next, Methyltetrazine-benzylamine·HCl (2.99 mg, 0.0126 mmol, 0.08 eq.) was added, letting the solution stirring for 72 hours. The solution was purified by precipitation in absolute ethanol (5 × 200 mL) followed by 24 hours of dialysis (membrane cut off 10 kDa) against water. The dialyzed product was then freeze-dried obtaining a pink amorphous product, characterized by ^{1}H NMR and UV-Vis spectrometry.

Yield: 94 % w/w

Thiolated Paclitaxel (PTX-SH)

Mercaptopropionic acid (10.87 mg, 0.118 mmol, 1 eq.) was dissolved in DMF. Next, DCC (24.35 mg, 0.118 mmol, 1 eq.) was added to the solution with PTX (50 mg, 0.059 mmol, 0.5 eq.) and a catalytic amount of DMAP. The mixture was then stirred for an hour in an ice bath, followed by 24 hours at 40 °C. Next, the mixture was filtered under vacuum, resuspended in DMF, and then precipitated in petroleum ether (5 × 200 mL). The product was then freeze-dried and characterized by ^{1}H NMR, ^{13}C NMR, Mass Spectrometry and Elemental Analysis.

Yield: 49% w/w

Hyaluronic Acid-Pyridyl Disulfide Cisteamine-Tetrazine-Paclitaxel (HA-PD-Tz-PTX)

HA-PD-Tz (80 mg, 0.110 mmol, 1 eq.) was dissolved in 25 mL of ultrapure water. PTX-SH (5.18 mg, 0.0055 mmol, 0.05 eq.) was solubilized in 2 mL of DMF and then added to the polymer. The mixture was stirred for 24 hours at RT. After that time, the mixture was purified by precipitation in absolute ethanol (5 × 200 mL) followed by 24 hours of dialysis (cut off membrane 10 kDa) against water. The final product was then freeze dried obtaining a pink amorphous product that was then characterized by ^{1}H NMR and UV-Vis analysis.

Yield: 85% w/w

Hyaluronic Acid-Pyridyl Disulfide Cisteamine-Paclitaxel (HA-PD-PTX)

HA-PD (80 mg, 0.139 mmol, 1 eq.) was solubilized in 25 mL of ultrapure water at RT. PTX-SH (6.59 mg, 0.007 mmol, 0.05 eq.) was dissolved in 2 mL of DMF and then the solution was added to the polymer. Next, the mixture was stirred for 24 hours followed by purification including precipitation in absolute ethanol (5 × 200 mL) and 24 hours of dialysis (cut-off membrane 10 kDa) against water. The final product was freeze-dried. The white product obtained was characterized by ^{1}H NMR.

3.2.2. Synthesis of PLL conjugate

Poly-L-Lysine-Trans-Cyclooctene (PLL-TCO)

PLL (300 mg, 2.29 mmol, 1 eq.) was dissolved in 50 mL of borate buffer (pH=9) and was added to a solution of TCO-NHS (30.6 mg, 0.1145 mmol, 0.05 eq.) previously dissolved in 4 mL of DMSO. The mixture was stirred for 24 h at RT. The final PLL-TCO product was purified by 24 hours of dialysis (membrane cut off 1 kDa) against water. The final solution containing purified PLL-TCO was then freeze-dried and analysed by ^{1}H NMR and UV-Vis spectrometry.

Yield: 74% w/w.

3.3. Synthesis of HAPLL Nanoparticles (NPs)

Small batch protocol

Preparation of 1:1 ratio HAPLL NPs

PLL (1 mg/mL, 4 mL) was mixed with HA (1 mg/mL, 4 mL). To assemble the nanoparticles, a microfluidic-based nanoassemblr, NE-1000 SyringeONE Programmable Syringe Pump (Darwin Microfluidics, Austin TX, USA), was used, with a flow rate of 12 ml/min and a flow rate ratio of 1:1. 4 ml of each solution was put in 5 ml syringes and a final solution of 7.5 ml of NPs was obtained. The final product was then characterized by DLS in ultrapure water and in PBS.

Preparation of 10:1 ratio HAPLL NPs

PLL (0,2 mg/mL, 4 mL) and HA (2 mg/mL, 4 mL) were used to formulate the nanoparticles. The solutions were put in two different 5 mL syringes and mixed using a microfluidic-based nanoassemblr, obtaining a final solution of 7.5 mL, characterized by DLS in water and in PBS. The flow rate was 12 mL/min and a flow rate ratio of 1:1 was used.

Preparation of 1:1 ratio CL HAPLL NPs

PLL-TCO (1 mg/mL, 4 mL) was mixed with HA-Tz (1 mg/mL, 4 mL) using a microfluidic-based nanoassemblr, with a flow rate of 12 mL/min and a flow rate ratio of 1:1. 4 mL of each solution was put in 5 mL syringes and a final solution of 7.5 mL of NPs was obtained and subsequently characterized using DLS analysis in ultrapure water and in PBS.

Preparation of 10:1 ratio CL HAPLL NPs

Nanoparticles were formulated using PLL-TCO (0.2 mg/mL, 4 mL) and HA-Tz (2 mg/mL, 4 mL), each loaded into separate 5 mL syringes. A pump-based nanoassemblr with a flow rate of 12 mL/min and a 1:1 flow rate ratio mixed the solutions, resulting in a final volume of 7.5 mL. Obtained nanoparticles were then analysed by DLS water and in PBS.

Preparation of 10:1 ratio CL HAPLL NPs-PTX

To prepare the nanoparticles, PLL-TCO (0.2 mg/mL, 4 mL) and HA-PD-Tz_PTX (2 mg/mL, 4 mL) were loaded into individual 5 mL syringes and mixed with a microfluidic-based nanoassemblr, with a flow rate of 12 mL/min and an equal flow rate ratio of 1:1. The final volume was 7.5 mL of nanoparticles solution, that was then characterized by DLS analysis in water and PBS.

Big batch protocol

Preparation of 10:1 ratio CL HAPLL NPs

HA-Tz (5 mg/mL, 15 mL) and PLL-TCO (0,5 mg/mL, 15 mL), were put in two different syringes and mixed using a microfluidic-based nanoassemblr. The flow rate was 12 mL/min with a flow rate ratio of 1:1. 19.5 mL of the final solution was obtained, freeze-dried and further characterized.

Preparation of 10:1 ratio CL HAPLL NPs-PTX

HA-PD-Tz-PTX (5 mg/mL, 15 mL) and PLL-TCO (0.5 mg/mL, 15 mL) were loaded into separate syringes and mixed with a pump-based nanoassembler. A flow rate of 12 mL/min with a 1:1 ratio was used, yielding 19.5 mL of the final solution, freeze-dried and further characterized.

3.4. Chemical-Physical Characterization

Nuclear Magnetic Resonance (NMR) Spectroscopy Analysis

Each product or intermediate was analyzed by ^{1}H NMR. Firstly 3.0 mg of each sample were measured and dissolved in 600 µL of the proper deuterated solvent. Next, the solution was put in a proper NMR glass tube. The samples were then processed using Evolution 201 spectrometer by Thermo Scientific (Madison, WI, USA) 400 MHz instrument. The analysis of the spectra was carried out using MestreNova software from Mestrelab.

UV-Visible Spectrophotometric Analysis

Spectrophotometric analysis was used to quantify the amount of Methyltetrazine-benzylamine·HCl conjugated to HA polymers. Tz solutions (1 mL) at different and known concentrations (5-600 µg/mL) were prepared and their absorbance at 520 nm was investigated to obtain a calibration curve. Subsequently, sample solutions at known concentrations were prepared and their absorbance at 520 nm, the absorbance wavelength of tetrazine, was measured. After that, using the linear interpolation

of the calibration line, the amount of Tetrazine conjugated to the analyzed sample was obtained. The analysis was performed in triplicate. An Evolution 201 spectrometer by Thermo Scientific (Madison, WI, USA) instrument was used.

Mass Spectrometry Analysis

To measure the m/z charge of ions, which provides information about the molecular weight and structure of the analysed molecules (PTX-SH and PD), 40 µL of a solution 5 mg/mL of the samples were analysed by an Evolution 201 spectrometer by Thermo Scientific (Madison, WI, USA).

Elemental Analysis

Elemental analysis was used to investigate the elemental composition of PTX-SH. 10 mg of the sample were collected. The analysis was done supported by Dr. Michela Paccagnella (Department of Pharmaceutical and Pharmacological Sciences, University of Padova) using a VarioMicro Cube with Autoassembler bought from Elementar Analysensysteme GmbH (Langenselbold, Germany).

Dynamic Light Scattering Analysis - DLS

The size by number and the PDI of investigated nanoparticles were obtained using a Zetasizer Ultra (Malvern Panalytical, Worcestershire, UK) instrument. Analysis was performed in water, PBS and CSF, by doing solution 1 mg/mL of nanoparticles in the desired solvent. 400 µL of those solution were put in the specific cuvette and then analysed by the instrument. Analysis were performed in triplicate at room temperature.

Zeta potential

To investigate the charge of the nanoparticles, 800 µL of a 1 mg/mL solution of the sample in water were put in a proper cuvette and then analysed with the DLS instrument. Analysis were performed in triplicate at room temperature.

Transmission Electrons Microscopy Analysis - TEM

Transmission Electron Microscopy (TEM) samples were prepared by dissolving the required nanoparticles in PBS, obtaining a 1 mg/mL solution of each sample. All measurements, including particle size distributions, were analysed using ImageJ software (National Institutes of Health, Bethesda, MD, USA).

Stability Studies

Three different solutions were prepared: 1) in water, 2) in PBS mimicking the physiological conditions and 3) in CSF to prove the stability of the nanoparticles in a cerebral environment. The solutions were in a concentration of 1 mg/ml, both CL HAPLL NPs and CL HAPLL NPs. The ones in water were stocked at a 4°C temperature, while the ones in PBS and CSF were stocked at 37 °C. Their size was investigated after 24, 48, and 72 hours using the DLS. Analysis were performed in triplicate. The size of the different types of nanoparticles was measured also after lyophilization, resuspending the nanoparticles in ultrapure water and in PBS.

3.5. In vitro studies

Cell Line

Murine glioma SB28 cells (DSMZ, German Collection of Microorganisms and Cell Cultures GmbH, Leibniz Institute, Braunschweig, Germany) were cultured in Dulbecco's modified Eagle's medium (DMEM) with L-glutamine, 4.5 g/l D-glucose, and 1 mM sodium pyruvate at 37 ◦C in a 5% CO_2 atmosphere. The medium was supplemented with 10% of fetal bovine serum (FBS) and 1.0% of antibiotics (penicillin/streptomycin).

Cell Viability Assay – Crosslinked Nanoparticles

Murine glioma SB28 cells were seeded (3×10^3 cells/well) in 96-wells plate in 150 µL of Dulbecco's modified Eagle's medium (DMEM). After 24 hours, the medium was removed and the cells were treated with 150 µL of different concentration solutions of CL NPs (0.5 - 200 µg/mL). After seventy-two hours, the NPs solutions were removed and the wells were filled with an MTT solution at 0.5 mg/mL. The cells were then incubated for 3 hours at 37°C. After this period, the MTT solution was removed and 150 µL of DMSO was added to each well, leaving the plates on a shaker for an additional

30 min. At the end of this time, the wells were analysed using a UV-Vis spectrophotometer analysing their absorbance at a fixed wavelength of 560 nm. Data of treatment were compared with the untreated group, normalized as the 100% cell viability. The experiment was repeated three times under consistent conditions.

Cell Viability Assay – Paclitaxel

Murine glioma SB28 cells were seeded (3×10^3 cells/well) in 96-wells plate in 150 µL of Dulbecco's modified Eagle's medium (DMEM). Cells were treated with Paclitaxel concentrations (0.0001-5 µM) and incubated for 72h. Following this time, an MTT assay was performed. The experiment was repeated three times under consistent conditions.

4. Results and discussion

4.1. Preparation and characterization of HA-PLL Nanoparticles

In this project, we aimed to create polymer-based nanoparticles (NPs) for the local treatment of GBM. This delivery system was devised aiming to release the therapeutic agent in a controlled manner at the injection site while maintaining size and set of properties (such as physiological stability and brain penetration) enabling effective diffusion within the brain parenchyma to reach infiltrating GBM cells and without provoking healthy tissue damage. The polymers selected for preparing the NPs were HA and PLL, owing to their biocompatibility, biodegradability and non-toxicity [114]. As mentioned before, HA has a natural affinity for CD44, a receptor expressed throughout the body but significantly overexpressed in GBM cells [115]. On the other hand, CD44 is less express in neurons ensuring superior targeting towards cancer cells. This property allows for active targeting of the NPs to tumor cells. HA, as a polyanionic polymer, also has the advantage of spontaneously assembling with PLL, a polycationic polymer.

The first formulation was prepared taking advantage of the opposite HA and PLL charges to form NPs through simple electrostatic interactions. HA and PLL were combined using a microfluidic device. Two batches of NPs were prepared, differing in the initial concentrations of the polymer solutions. In the first batch, 1 mg/mL HA was mixed with 1 mg/mL PLL, yielding nanoparticles with a 1:1 polymer ratio. The second batch employed a 0.2 mg/mL PLL solution and a 2 mg/mL HA solution to achieve a 1:10 ratio. All components were prepared in an aqueous medium due to their solubility. Analysis via DLS (reported in *Figure 4*) indicated particle sizes of 13.06 nm for the 1:1 batch and 27.77 nm for the 1:10 batch, meeting the design criterion of sub-100 nm dimensions for optimal diffusion in GBM tissue [112].

However, stability tests in PBS (to simulate physiological conditions) revealed significant size increases for both batches (588.3 nm for the 1:1 ratio and 768.5 nm for the 1:10 ratio). This behavior it has been associated with the disruption of the electrostatic interactions stabilizing the NPs in physiological media, as high ionic strength perturbed or broke these interactions, leading to particle disaggregation. Given these findings, the design of an alternative nanoparticle system with stronger, physiologically stable interactions between the polymers was pursued to foster clinical applicability.

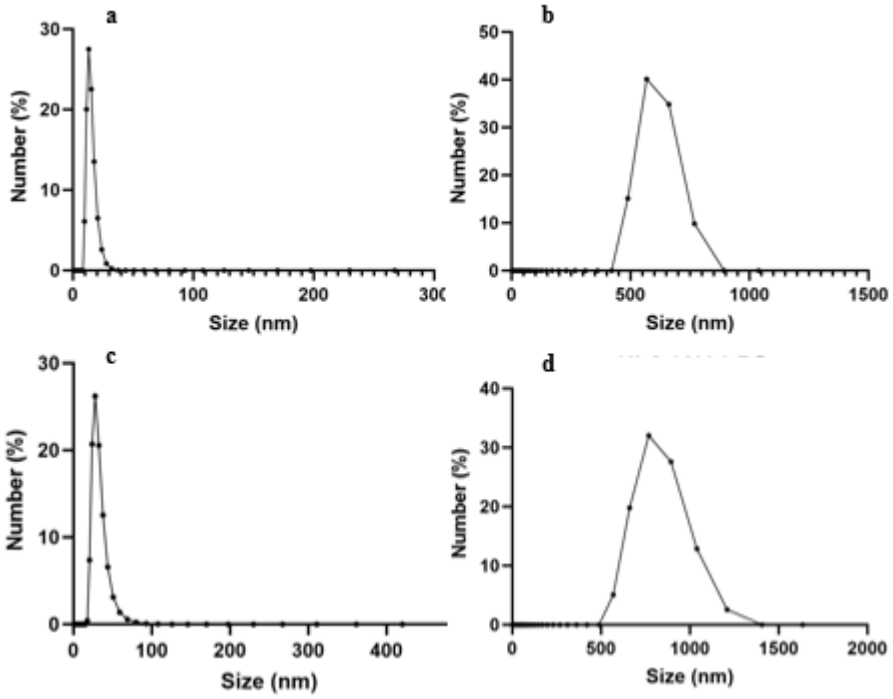

***Figure 4**: DLS analysis of HAPLL NPs 1:1 in **a)** mQ water, **b)** PBS (b), NPs 10:1 in water (c) and PBS (d)*

4.2. Design of Crosslinked Nanoparticles (CL HAPLL NPs)

Since NPs assembled via simple coulombic interactions between the polyanionic polymer HA and the polycationic polymer PLL did not provide sufficient stability under physiological conditions, it was necessary to explore alternative methods for their formulation. A chemical crosslinking approach was investigated to overcome this limitation. Hyaluronic acid, with its abundance of carboxylic groups, offers multiple functional sites for conjugation, while PLL can utilize its amine groups for similar purposes, making both polymers suitable for modification. The crosslinking strategy involved the derivatization of HA with Tetrazine while PLL was functionalized with Trans CycloOctene (TCO). These molecules were specifically selected due to their ability to form bioorthogonal links, which are characterized by high specificity and selectivity and biocompatibility in vitro and in vivo. Indeed, this linking chemistry is widely employed in clinical applications due to its reliability and safety profile. Moreover, the Tz-TCO reaction occurs rapidly in aqueous solutions, where the polymers are soluble, and at low concentrations, simplifying the formulation process.

To achieve crosslinked NPs with enhanced stability, the base polymers were chemically modified: HA was conjugated with Tz, and PLL with TCO. This design ensures a robust crosslinking

network between HA and PLL, addressing the stability issues encountered with electrostatically assembled nanoparticles while maintaining compatibility with physiological environments.

4.2.1. Synthesis and characterization of HA-Tz

The conjugation of Tz to HA utilized the abundance of carboxylic groups naturally present in the polymer. These groups, once activated, can react with amines to form stable amide bonds. To carry out the reaction, DMTMM was used as coupling agent, facilitating the formation of an intermediate that enhances the reactivity of the carboxylic acids.

After activation, Tz, which contains a primary amino group, was added to the solution. The amino group of Tz reacts with the activated carboxylic acids of HA, resulting in the formation of a covalent amide bond. This process effectively attaches Tz to the HA backbone. The reaction scheme, illustrating the underlying chemical mechanism, is shown in *Figure 5*.

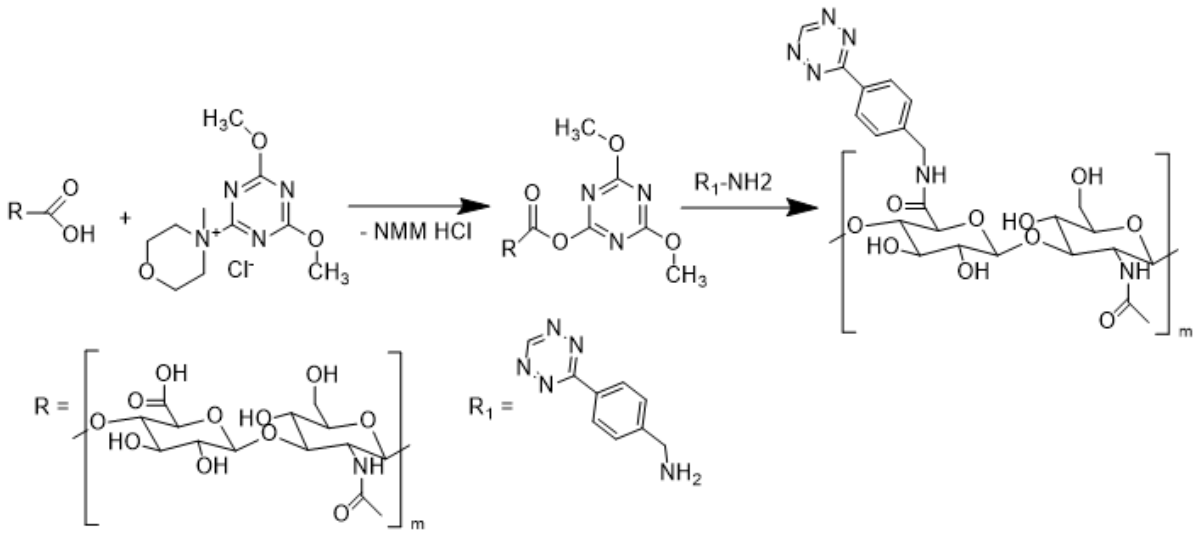

***Figure 5**: Chemical reaction between HA and Tz with a DMTMM coupling. Reaction was carried out at RT for 72 hours.*

At the end of the reaction time, the purification of the reaction mixture was carried out using ethanol precipitation. This step is used to remove unreacted Tz, which remained unbound to the polymer chain. During the initial stages of the purification process, the supernatant exhibited a bright pink colour, clearly indicating the presence of a substantial amount of free Tz. With repeated rounds of precipitation, the colour of the supernatant gradually faded, eventually becoming transparent, signifying the effective removal of unreacted Tz from the solution.

After purification, the product was then subjected to dialysis for 24 hours using a membrane with a molecular weight cut-off of 100 kDa. This step allowed for the diffusion of any remaining Tz or other low Mw impurities out of the solution, ensuring the purity of the conjugated polymer.

Finally, the purified product was lyophilized to obtain a dry, pink amorphous mass. This final material was subsequently characterized to confirm the success of the conjugation reaction and assess its properties.

As a first step, the loading capacity was evaluated to quantify the amount of Tz effectively conjugated to the polymer. This analysis leveraged a distinctive spectrophotometric property of Tz: its absorption band at 520 nm, a wavelength at which HA does not absorb. This allowed the direct measurement of the absorbance of the synthesized sample at 520 nm. Using a previously constructed calibration curve, the concentration of Tz within the polymeric sample was determined.

The calibration curve was generated by preparing Tz solutions at known concentrations ranging from 5 µg/mL to 600 µg/mL and measuring their absorbance at 520 nm. Each concentration was analyzed in triplicate to ensure reproducibility and the mean absorbance values were used to construct the curve. The calibration curve and its corresponding equation are presented in *Figure 6*.

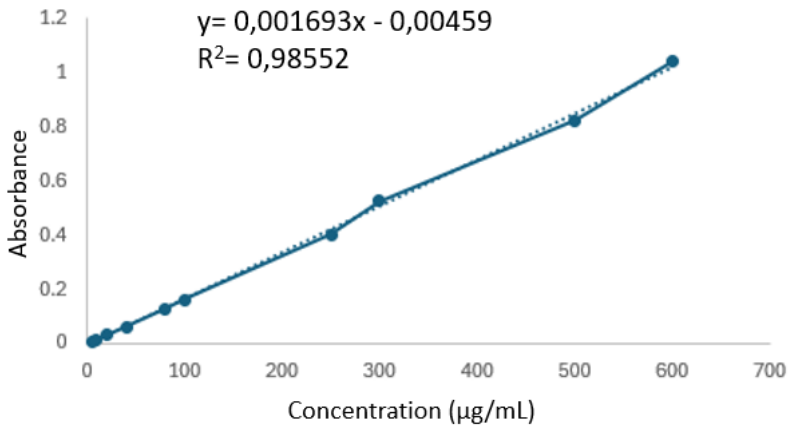

***Figure 6**: Calibration curve of Tz and relative equation.*

To quantify the Tz conjugated to HA, samples at known concentrations were analysed and their absorbance values were interpolated on the calibration curve. This enabled the determination of the average concentration of Tz in each sample and, subsequently, the calculation of the product's loading capacity, which was found to be 3.60%. Given that the reaction employed 5% Tz relative to the amount of HA, the conjugation efficiency was considered satisfactory.

An additional synthesis was performed to assess whether increasing the Tz ratio in the initial reaction mixture could enhance loading capacity. The HA:Tz ratio was adjusted from 100:5 to 100:8, and the resulting product was analysed using the same calibration curve methodology. However, the loading capacity remained nearly constant, averaging 3.65%. This minimal increase in conjugation efficiency did not justify the additional consumption of Tz. Therefore, subsequent synthesis retained the original 100:5 ratio, as increasing the Tz ratio resulted in negligible improvement in conjugation efficiency while increasing material waste.

The ^{1}H NMR spectrum of HA-Tz in D_2O, shown in *Figure 7*, was analyzed to verify the structural integrity of the synthesized compound. The results confirmed that the obtained product corresponded to the expected structure, providing evidence for the successful completion of the synthesis.

- A peak at 2.01 ppm was assigned to the methyl group in the polysaccharide chain, which is characteristic of HA;
- the series of peaks observed between 3.27 ppm and 4.00 ppm were identified as the hydrogens of the polysaccharide backbone;
- two distinct peaks at 7.67 ppm and 8.47 ppm were observed, which correspond to the hydrogens of the aromatic ring of the tetrazine moiety. These peaks serve as specific markers of the successful conjugation of tetrazine to HA.

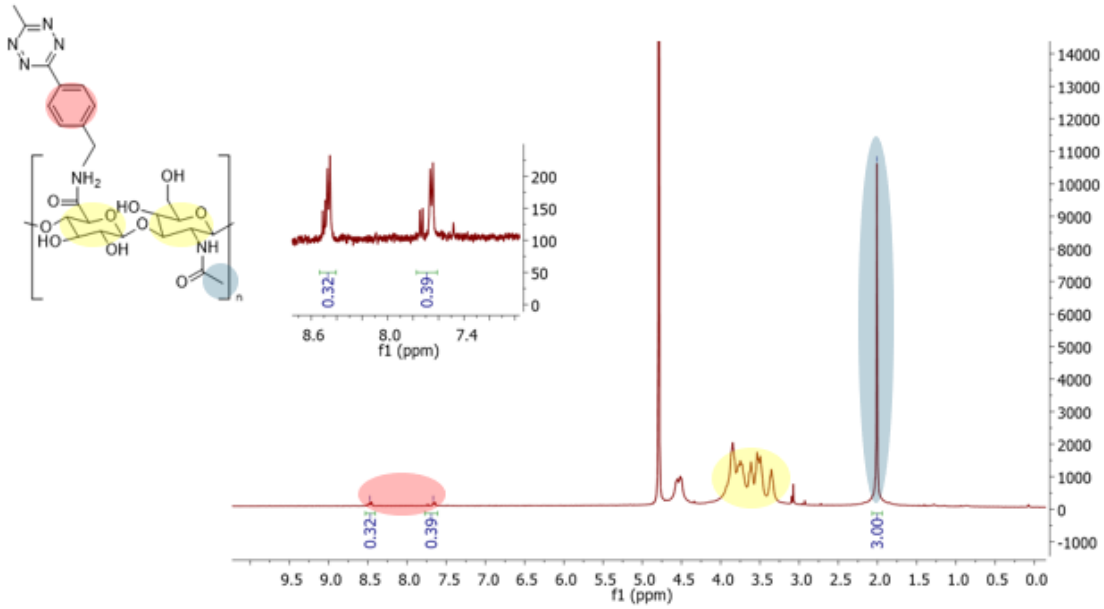

***Figure** 7: ^{1}H NMR spectrum of HA-Tz in D_2O. Colors on the structure represents the attributed peaks on the spectrum*

Finally, the reaction molar yield, calculated after the purification and lyophilization of the product, was 78%. The yield was calculated from the percentual ratio between the moles of the obtained product and the moles of the initial HA.

4.2.2. Synthesis and characterization of PLL-TCO

The TCO-NHS ester ensures specific and rapid reaction with primary amines, such as those located on the side chains of PLL, as represented in *Figure 8*. The availability of these amines for interaction with NHS-TCO and subsequent covalent bond formation depends on their being in a non-protonated state. To achieve this, the reaction was conducted in the presence of a borate buffer, which ensured the maintenance of an optimal pH environment, typically ranging between 7 and 9. This pH range promotes the deprotonation of the primary amine groups, facilitating their efficient reaction with NHS-TCO. Following the reaction, the mixture was subjected to a 24-hour dialysis process to remove any unreacted NHS-TCO. The dialysis was performed with a suitable membrane to allow the diffusion of small molecular weight impurities while retaining the modified polymer.

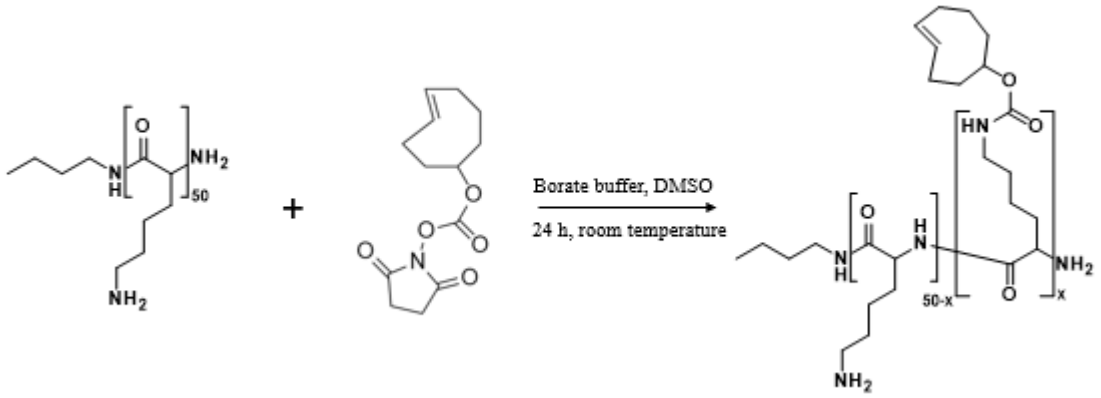

Figure 8. *Reaction scheme between PLL and NHS-TCO. The reaction was performed in borate buffer at pH 9.4*

The purified product was subsequently lyophilized, yielding an amorphous, white material. To confirm the successful modification of PLL and to analyze the chemical structure of the product, characterization was performed using spectrophotometry and ^{1}H NMR. These techniques provided detailed insights into the molecular composition and ensured that the desired reaction had occurred as intended.

The first step in characterizing the PLL-TCO polymer was to verify the successful conjugation of TCO to the PLL backbone using spectrophotometric analysis. TCO is known to exhibit a distinct absorption peak at 210 nm. Although this peak is not highly intense, it remains sufficiently detectable

to confirm its presence. On the other hand, the unmodified PLL polymer does not absorb at this wavelength, making the comparison straightforward.

To assess the presence of TCO in the freshly synthesized sample, the absorbance spectrum of PLL-TCO was recorded and compared with that of unmodified PLL. As illustrated in *Figure 9*, the spectrum of PLL-TCO reveals an absorption shoulder at 210 nm, which is absent in the spectrum of bare PLL. This difference in absorption profiles strongly suggests the successful conjugation of TCO to the PLL polymer.

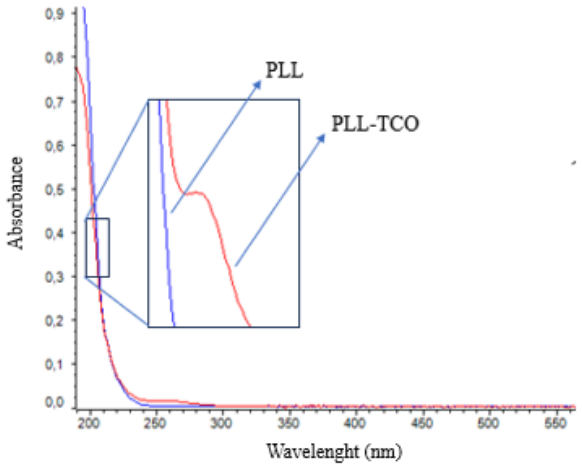

Figure 9: *Spectrophotometric analysis of PLL and PLL-TCO, highlighting shift absorbance of PLL-TCO.*

In addition to spectrophotometric analysis, a ^{1}H NMR characterization of PLL-TCO was performed and the resulting spectrum is presented in *Figure 10*. The NMR analysis was carried out using an aqueous solvent, D_2O. The spectrum reveals three significant peaks, each corresponding to specific structural components of the PLL-TCO conjugate:

- A series of peaks between 1.2 ppm and 1.7 ppm, representing the protons of the alkyl side chains in the PLL backbone;
- a distinct peak at 4.29 ppm, integrating for one proton, attributed to the hydrogen of the anomeric carbon of the amino acid unit;
- two peaks at 5.54 ppm and 5.68 ppm, which correspond to the protons associated with the double bond within the octane ring of TCO.

While this NMR analysis was not performed with the intention of quantifying the amount of TCO conjugated to PLL, it serves as a qualitative indicator of the successful reaction. The presence of the

characteristic TCO peaks confirms that TCO is conjugated to the PLL polymer and provides further evidence supporting the efficiency of the synthesis process.

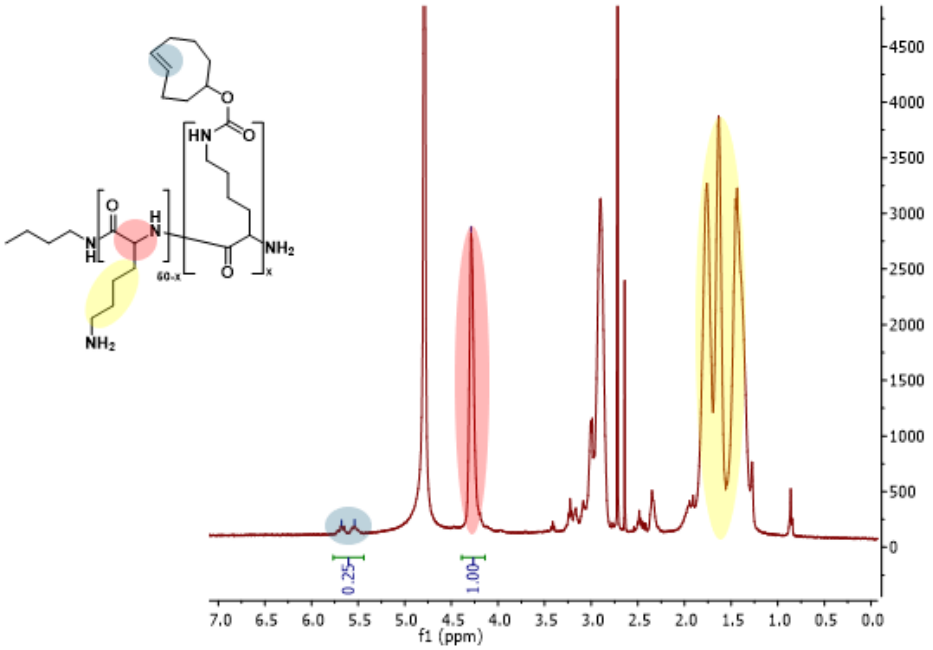

***Figure 10**: [1]H NMR spectrum of PLL-TCO in D_2O. Colors on the structure represent the attributed peaks on the spectrum.*

Finally, the reaction molar yield was 74%. The yield was calculated from the percentual ratio between the moles of the obtained product and the moles of the initial PLL.

After confirming the conjugation of HA and PLL with Tz and TCO, respectively, the formulation of crosslinked nanoparticles was carried out. The covalent bond between Tz and TCO is formed through an inverse-electron demand Diels-Alder cycloaddition reaction (shown in *Figure 11a*). This reaction is bioorthogonal and exhibits exceptional kinetics (rate constants up to 10^6 M^{-1} s^{-1})[124]. The rapid kinetics, combined with the high specificity of the reaction, enables the conjugation of these molecules even at low concentrations, resulting in the formation of a stable dihydropyridazine structure.

To confirm the successful formation of the covalent bond and the synthesis of the CL HAPLL NPs, an [1]H NMR analysis was conducted and the spectrum is reported in *Figure 11b*. The results confirmed the presence of characteristic peaks associated with HA and PLL molecules, indicative of their presence within the structure. In particular:

- a peak at 2 ppm was attributed to the three protons of the methyl group attached to the polysaccharide chain;

- a series of peaks in the range of 3.25–3.75 ppm were assigned to the protons along the HA backbone;
- at 4.29 ppm, a peak corresponding to the proton of the anomeric carbon in the PLL chain was detected;
- in the range of 7.5–8.5 ppm, characteristic peaks of the aromatic ring of tetrazine were observed;
- notably, the signal corresponding to the double bond of the trans-cyclooctene at 5.2 ppm was absent.

This absence confirms the reaction between Tz and TCO, as this region is directly involved in the reaction, leading to the disappearance of the trans cyclooctene signal from the ^{1}H NMR spectrum of the CL HAPLL NPs.

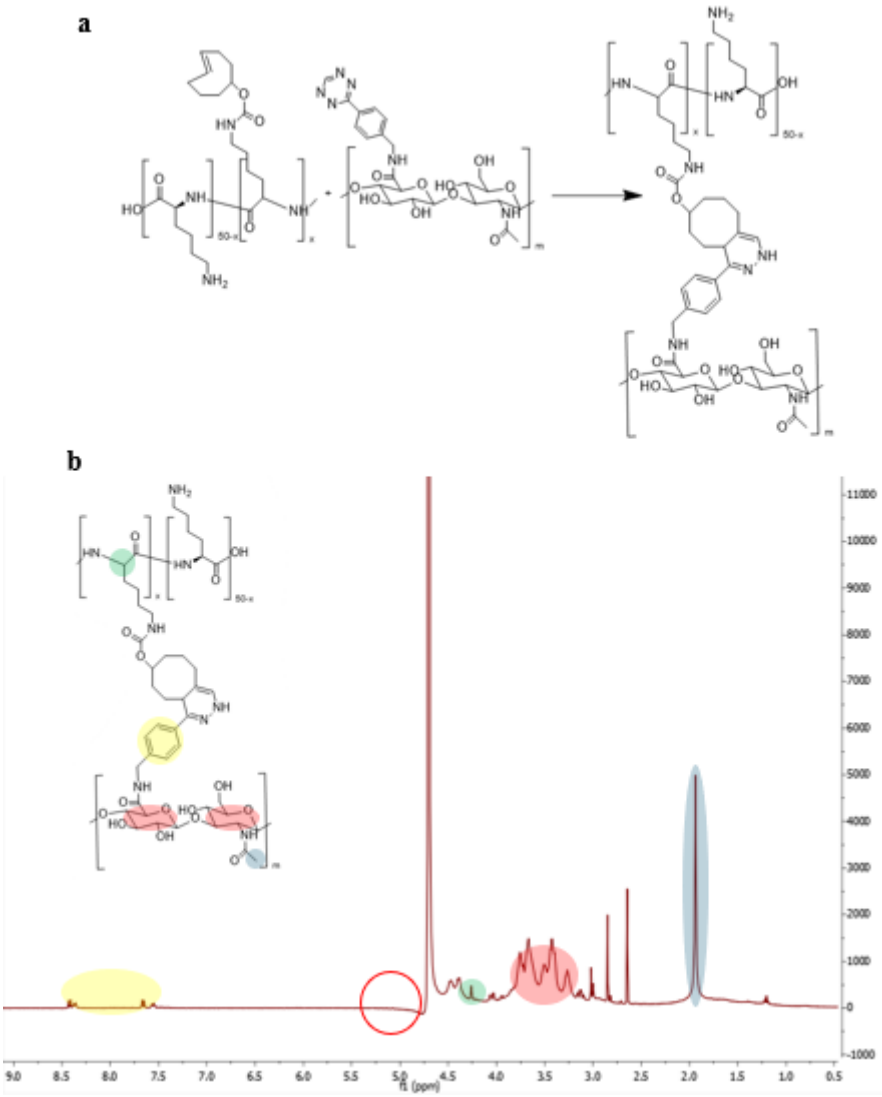

***Figure 11**: Reaction between Tz and TCO leading to the formation of a covalent bond (a), ^{1}H NMR spectrum of CL HAPLL NPs in D_2O (b). Colors in the structure highlight the corresponding peaks in the spectrum.*

To optimize the formulation of crosslinked nanoparticles (CL NPs), two distinct ratios of the HA-Tz and PLL-TCO polymers were tested: 1:1 and 10:1.

Synthesis of CL HAPLL 1:1

Aqueous solutions of HA-Tz and PLL-TCO at concentrations of 1 mg/mL, respectively were introduced into a pump-driven microfluidic system. This resulted in a solution containing nanoparticles, which were immediately analyzed by dynamic light scattering (DLS) to assess their size. The measured diameter was 37.56 nm (reported in *Figure 12a*), aligning with the expected and desired particle size.

To evaluate their potential for the intended application, the stability of these particles in a saline environment was investigated by measuring their size in PBS using DLS (reported in *Figure 12b*). Unfortunately, this analysis revealed a significant increase in size achieving a diameter of 488.7 nm, indicating that the particles behaved as though they were not crosslinked. To address the possibility that Tz and TCO had not reacted to form the desired bioorthogonal bond, an observation was considered: the solution lost its characteristic pink color, suggesting Tz had reacted.

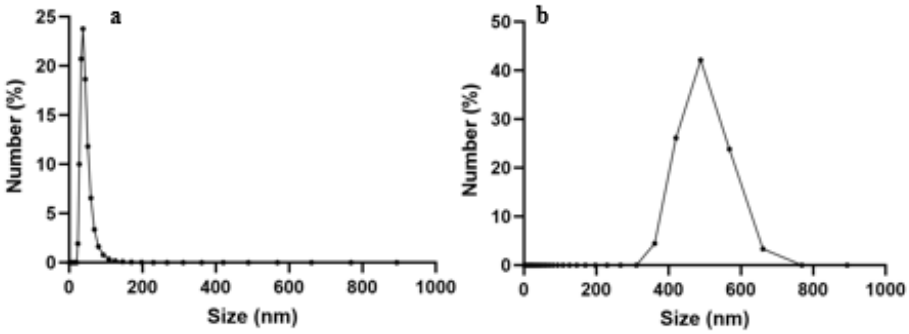

***Figure 12**: Dimension analysis of CL HAPLL 1:1 in water (a) and in PBS (b)*

Synthesis of CL HAPLL 10:1

Given these findings, we hypothesized to increase the amount of HA-Tz, trying to improve the probabilities of reaction between Tz and TCO groups conjugated on the polymer chins. We prepared a novel formulation made of a 10:1 ratio of HA-Tz to PLL-TCO. The same protocol reported above was followed, with the concentrations adjusted to 2 mg/mL for HA-Tz and 0.2 mg/mL for PLL-TCO. The resulting NPs were analyzed by DLS, and their size was found to be approx. 50.00 nm. Interestingly, we observed that after switching the medium from water to PBS, these NPs retained the size with a small shrink to 43.68 nm, suggesting stability (*Figure 13*). This improved stability makes the 10:1 formulation a more suitable candidate for potential exploration in future tests. Following the

promising results obtained with the CL HAPLL NPs 10:1 formulation, further analyses were conducted exclusively on these particles, as the CL HAPLL NPs 1:1 formulation lacked stability and was deemed unsuitable for future exploration. To evaluate the feasibility of scaling up production, larger quantities and higher concentrations of the two starting solutions were tested while maintaining the optimal 10:1 ratio of HA-Tz to PLL-TCO. The process of scaling up is crucial as it facilitates the production of larger batches with higher concentrations, significantly saving time and resources in the laboratory. From a long-term perspective, scaling up is essential for transitioning the formulation of NPs from a small-scale laboratory process to a larger-scale production suitable for industrial applications. This transition is vital for enabling the widespread use and commercialization of such formulations in the pharmaceutical and biotechnology industries.

For the preparation of a larger batch of CL NPs, 15 mL of a 5 mg/mL HA-Tz solution and 15 mL of a 0.5 mg/mL PLL-TCO solution were mixed using the established microfluidic system. This process resulted in 19.5 mL of an aqueous nanoparticle solution.

Dimensional analyses and zeta potential analysis were conducted on this larger-scale formulation. The results confirmed a consistent particle size of 50.79 nm in aqueous solution and 43.68 nm in PBS, indicating both the scalability of the formulation and the stability of the particles in a saline environment. The resulting zeta potential was -50 mV.

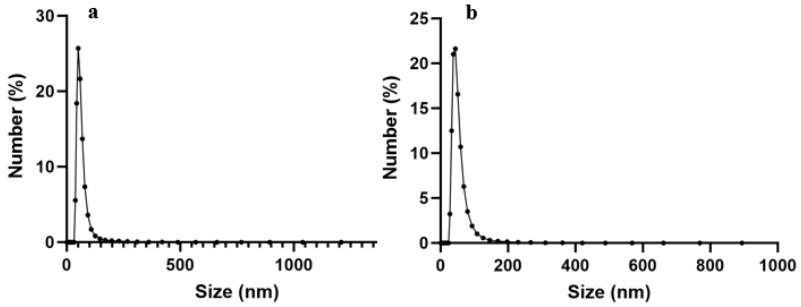

***Figure 13**: Dimensional analysis of CL HAPLL NPs 10:1 in mQ water (a) and in PBS (b), proving their stability in the physiological environment*

A stability study was performed to evaluate the behaviour of crosslinked nanoparticles under three different conditions: 1) PBS, 37°C, 2) PBS 4°C and 3) artificial Cerebral Spinal Fluid (CSF) at 37°C. The stability was assessed via dimensional analysis in these media at predefined intervals: immediately after preparation (time 0), and then at 24, 48, and 72 hours. This approach aimed to simulate clinical scenarios where the nanoparticle solution might not be immediately administered, thus requiring short-term storage without compromising its properties. Given that these nanoparticles are intended for local administration via local injection, it is possible that during surgical procedures,

unforeseen delays might occur, leaving part of the prepared solution unused. Evaluating the stability of this residual solution under refrigeration is essential to reduce waste and ensure the practicality of this therapeutic approach.

The study confirmed that the NPs maintained their stability and structural integrity in a saline environment at 4°C for up to 72 hours, suggesting their robustness for potential clinical handling. Furthermore, the stability of the nanoparticles was assessed at physiological temperature (37°C) in PBS and CSF, two media chosen to mimic the ionic strength and saline concentration of biological fluids. In this experiment, the nanoparticle solutions were stored at 37°C, and their sizes were monitored at regular intervals over 72 hours.

This aspect of the study reflects a critical consideration for the intended application. When injected intracranially, the NPs may not be immediately internalized by cells but are likely to remain transiently within the brain parenchyma, interacting with cerebrospinal fluid and other physiological components. During this time, the nanoparticles are expected to diffuse and release the conjugated drug in a controlled manner. Stability under these conditions is therefore vital to ensure the system's efficacy; any disaggregation or alteration in size could compromise the drug's delivery and therapeutic potential. As illustrated in *Figure 14*, the crosslinked nanoparticles demonstrated excellent stability along the time, maintaining consistent size profiles under both refrigerated and physiological conditions for the full 72-hour duration of the analysis.

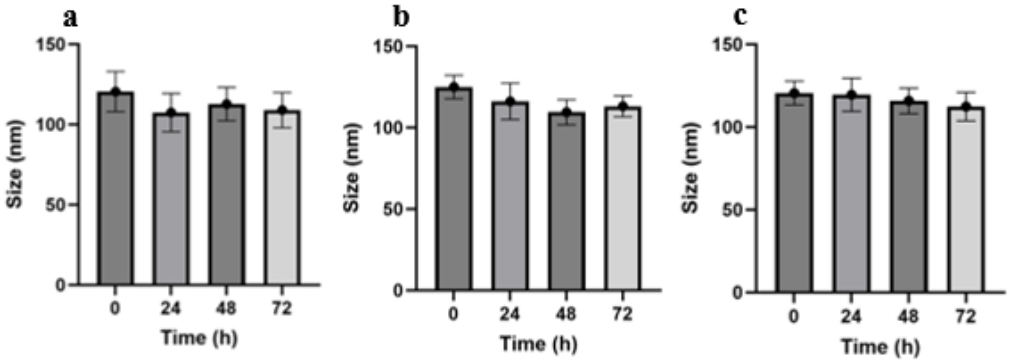

Figure 14: *Stability study of CL HAPLL NPs in different solvents: a) PBS at 4 °C, b) CSF at 37 °C, c) PBS at 37 °C.*

The morphology and particle size of the nanoparticles were thoroughly analysed using TEM (*Figure 15*). This technique provided a detailed visual confirmation of the dimensions and the morphology of NPs previously measured through DLS, ensuring consistency between the two methods. The TEM analysis revealed that the nanoparticles exhibit a nearly spherical shape and a high degree of homogeneity in size distribution. This indicates a successful synthesis and uniformity in their structural characteristics, a critical parameter for their intended application.

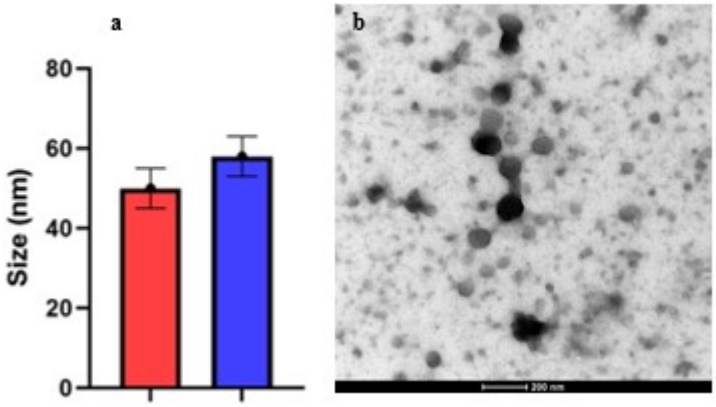

***Figure 15**: Particle size of CL HAPLL 10:1 NPs obtained with TEM analysis (red) and DLS analysis (blue) (a) and morphology obtained with TEM analysis (b). Scale bar is 200 nm.*

The investigations into the morphology and stability of the synthesized nanoparticulate system were crucial to evaluating its potential for application in physiological environments while preserving its therapeutic efficacy. However, to ensure clinical translation, the nanoparticles must exhibit biocompatibility and non-toxicity toward the cells they encounter. This is critical, as the cytotoxic effects should exclusively originate from the conjugated therapeutic agent, avoiding any intrinsic toxicity from the nanoparticle system itself.

Biocompatibility of HAPL NPs

To assess this aspect, an MTT assay was conducted to determine the viability of murine glioblastoma SB28 cells after exposure to CL NPs. The cells were incubated with varying concentrations (from 0.5 µg/mL to 200 µg/mL) of the NPs for 72 hours, followed by the MTT assay to measure cell viability. The assay involved the spectrophotometric reading of treated wells at 560 nm, reflecting the metabolic activity of the cells. The resulting data were analyzed using GraphPad Prism software.

This analysis confirmed the potential use of the nanoparticles, as they were demonstrated to be non-toxic to the glioblastoma cell line under the conditions tested (*Figure16*). These findings highlight the system compatibility with physiological conditions and support its further development as a safe platform for targeted drug delivery in glioblastoma treatment.

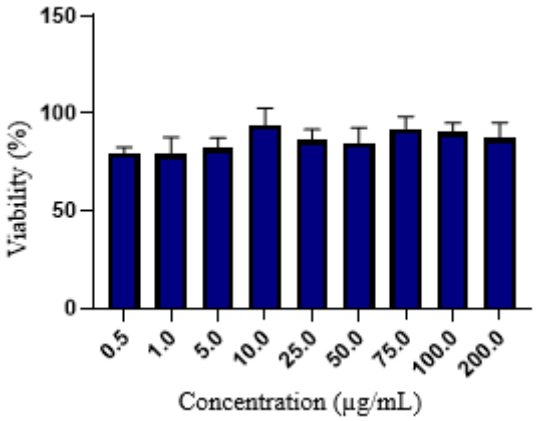

***Figure 16**: Cell viability of murine glioblastoma SB28 cell line incubated for 72 hours with various concentration of CL HAPLL NPs from 0.5 µg/mL to 200 µg/mL.*

4.3 Design of Crosslinked HAPLL Nanoparticles conjugated with PTX

After stability, and biocompatibility assessment of CL NPs 10:1, the nanoparticles were conjugated with Paclitaxel (PTX). PTX works by inhibiting cellular replication. Paclitaxel promotes the polymerization of tubulin into stable microtubules and directly interacts with these structures, stabilizing them against depolymerization induced by cold or calcium, which normally cause microtubule disassembly. This stabilization results in the arrest of cells in the G2/M phase of the cell cycle, preventing the formation of a functional mitotic apparatus [125]. This drug has been extensively studied in GBM therapy, where it has shown significant cytotoxic effects [126]. Despite its therapeutic potential, the clinical application of this drug has been significantly hindered by its poor ability to overcome the BBB, which limits its effective delivery to the central nervous system. These effects were corroborated in the present study through cell viability assays, as illustrated in Figure 17. In this experiment, murine GBM SB28 cells were incubated with a range of PTX concentrations, from 10^{-4} µM to 5 µM, for 72 hours. Viability was assessed using the MTT assay, with spectrophotometric readings at 560 nm providing quantitative measurements of cell survival,showing an IC_{50} of 10.20 nM. The results confirmed the pronounced cytotoxicity of PTX against GBM cells, reinforcing its relevance as a therapeutic agent in this context.

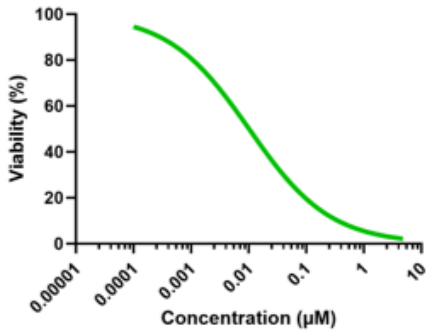

***Figure 17**: Correlation between cell viability and concentration of the PTX they were incubated with, showing that PTX exhibit high cytotoxic activity.*

Next, PTX was conjugated to HAPLL as reported in *Figure 18*. This conjugation was aimed at developing a bioresponsive linker designed to release the drug selectively under conditions characteristic of the tumor microenvironment. GBM is known to exhibit high intracellular levels of glutathione ten times higher than the extracellular concentration, a tripeptide that imparts strong reducing properties; thus, a linker incorporating a disulfide linker was developed, aiming to facilitate controlled PTX release specifically after cell uptake. This linker ensures that the chemotherapeutic agent remains inactive until it reaches the tumor site, thereby minimizing off-target effects and enhancing therapeutic precision.

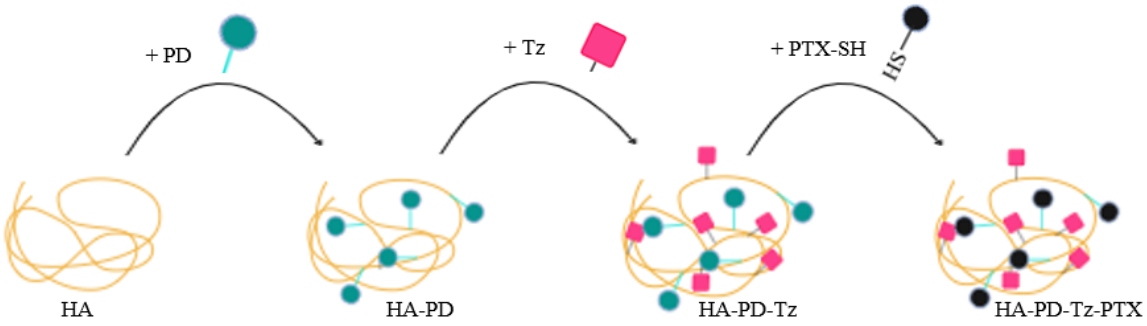

***Figure 18**: General schematics of the synthesis that will be further represented below*

4.3.1. Synthesis and characterization of Pyridyl Disulfide Cysteamine (PD)

The goal of this synthesis is to produce a linker between the HA polymer backbone and the thiol-functionalized PTX. Pyridyl Disulfide Cysteamine was selected due to its ease of synthesis, versatility and compatibility with the intended chemical modifications. The chemical pathway employed to synthesize Pyridyl Disulfide Cysteamine is illustrated in *Figure 19*.

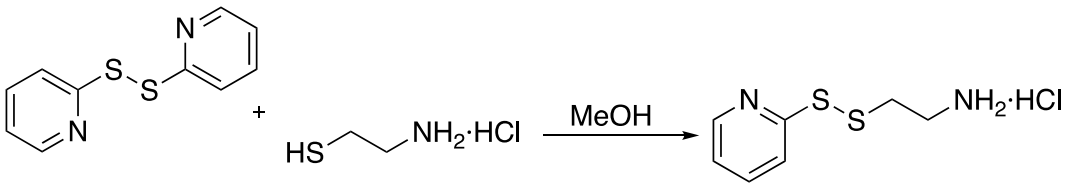

***Figure 19**: Synthesis of Pyridyl Disulfide Cisteamine. The reaction is conducted in MeOH under N_2 atmophere overnight at RT*

Following the end of the reaction, the product was purified by precipitation in diethyl ether to remove unreacted starting materials and by-products. The final compound was characterized comprehensively using mass spectrometry to confirm its molecular weight and structural analysis by ^{1}H NMR.

The mass spectrometry analysis, conducted using a TOF instrument in positive ionization mode, displays a primary peak at an m/z of 221.02, which corresponds to the molecular ion of the synthesized compound, as expected. Alongside the main signal, two secondary peaks are present at m/z 222.02 and 223.02, with relative intensities of 10% and 9%, respectively. These additional peaks are consistent with the isotopic distribution of the molecule and align with theoretical predictions. Results obtained are shown in *Figure 20a*.

The ^{1}H NMR spectrum (reported in *Figure 20b*) obtained further confirmed the successful synthesis of the target molecule. Two distinct groups of peaks are evident in the spectrum:

- the first group, located between 7 ppm and 9 ppm, corresponds to the aromatic protons of the pyridine ring;
- the second group of peaks, found between 2.9 ppm and 3.4 ppm, represents the protons of the alkyl chain present in the molecule, specifically the four protons attached to the carbon atoms in the alkyl segment.

This detailed spectral analysis supports the identification of the desired product, confirming both the pyridine and alkyl chain components in the structure.

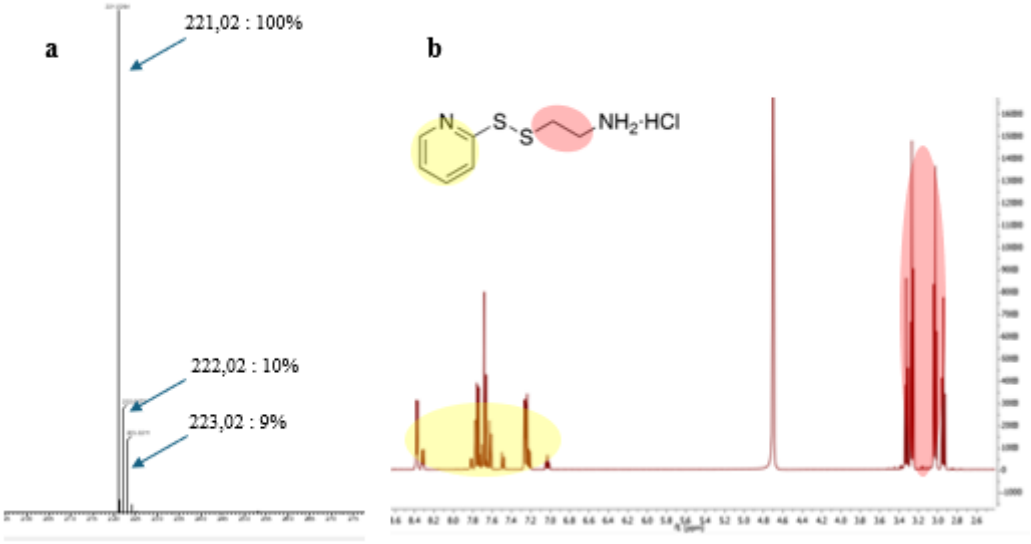

***Figure 20**: MS spectrum of PD, obtained by TOF method (a) and ^{1}H NMR spectrum (b). Colors on the structure represents the attributed peaks on the spectrum*

Finally, the molar yield of the reaction was determined, and the result indicated an 81% yield.

4.3.2. Synthesis and characterization of HA-PD

After confirming the successful synthesis of PD, this moiety was conjugated to the HA. PD possesses an amine group, which facilitates interaction with the activated carboxyl group of HA, resulting in the formation of a stable amide bond. This conjugation is facilitated by the use of DMTMM Cl, a reagent that activates the carboxyl group of HA, making it more reactive towards nucleophilic attack by the amine group. As a result, a covalent bond is formed between the HA polymer and the PD molecule. The schematic representation of this reaction is provided in Figure 21, which outlines the key steps involved in the conjugation process.

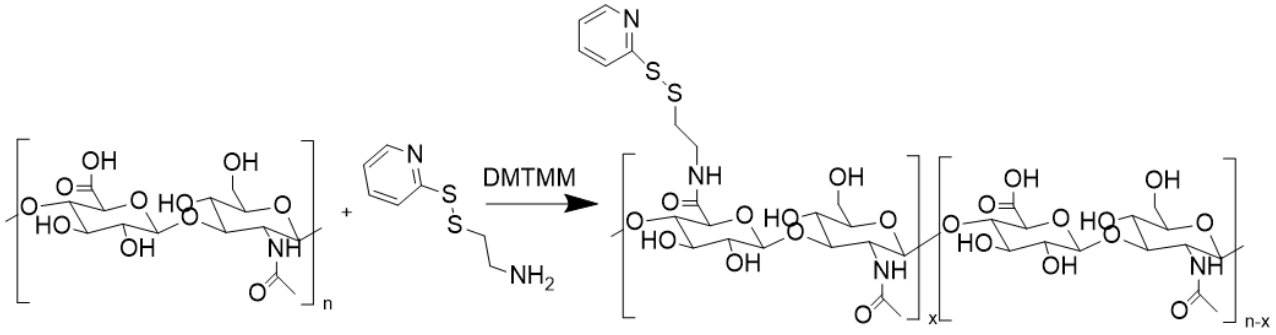

***Figure 21**: Chemical reaction between HA and PD with a DMTMM coupling. Reaction was carried out at RT for 72 hours.*

Following the synthesis and purification of the obtained product through dialysis, the lyophilized product underwent detailed characterization using NMR analysis. The resulting NMR spectrum, presented in *Figure 22*, clearly indicates the presence of all the expected components within the molecule under investigation.

- A distinct peak at 2 ppm, integrating for 3 protons, corresponds to the methyl protons related to the polysaccharide chain of HA;
- the region between 2.8 ppm and 4 ppm contains a complex set of peaks arising from the overlapping signals of protons from both the HA polymer chain and the 2-carbon alkyl chain of PD. This overlapping pattern is indicative of the presence of both the polysaccharide and alkyl components in the conjugate;
- a set of peaks in the range of 7.2 ppm to 8.4 ppm is observed, characteristic of the protons from the terminal pyridine ring, confirming the presence of the pyridine structure in the molecule.

This ^{1}HNMR analysis conclusively demonstrates that the synthesis was successful and proceeded as expected, thereby allowing the progression to the subsequent reactions needed.

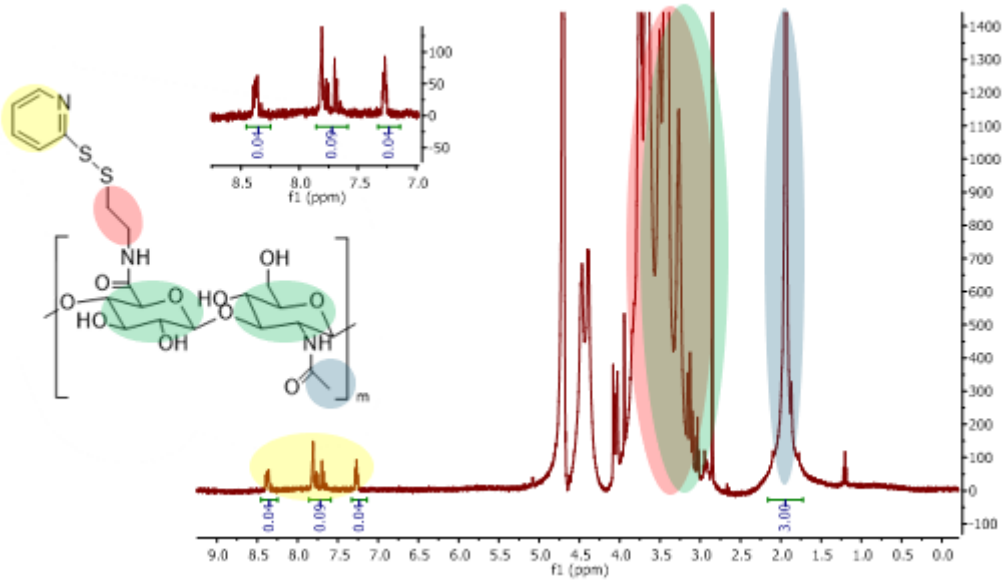

***Figure 22**: ^{1}H NMR spectrum of HA-PD. Colors on the structure represents the attributed peaks on the spectrum*

Finally, the mass yield of the reaction was calculated, obtaining a 95% yield.

4.3.3. Synthesis and characterization of HA-PD-Tz.

The next step in the synthesis was the conjugation of Tz to the HA-PD. Tz plays a critical role in the formation of crosslinking between HA and PLL-TCO during the NPs assembly process. The conjugation of Tz to the HA-PD polymer involves the chemical activation of the free carboxylic residues still present on HA. This activation is achieved using DMTMM Cl, a coupling reagent that promotes the formation of a stable amide bond between the carboxylic acid groups on the polymer and the amine group of the Tz molecule. The reaction scheme is resumed in *Figure 23*. Once the reaction was completed, unreacted reagents and by-products were removed through a sequential process of filtration and dialysis to ensure the purity of the final product. The purified product was then lyophilized, resulting in an amorphous, pink-colored powder, indicative of the successful incorporation of Tz into the HA-PD polymer chain.

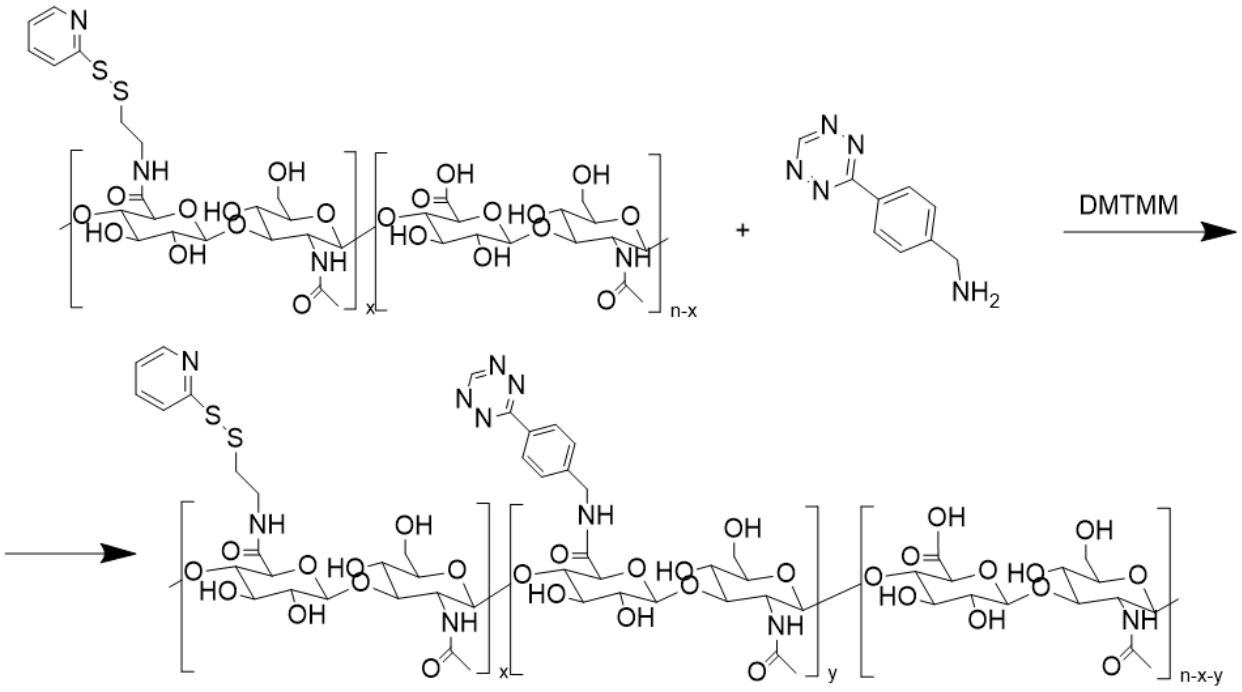

***Figure 23**: Scheme of the chemical reaction between HA-PD and Tz with a DMTMM coupling. Reaction was carried out at RT for 72 hours.*

The investigation into the HA-Tz conjugation was conducted by assessing its absorbance at 520 nm, the characteristic wavelength for Tz detection. By interpolating the absorbance value of the sample with an unknown Tz concentration into a calibration curve previously established, the Tz concentration in the sample was determined. This allowed for the calculation of the loading capacity, which was found to be, on average, 2.2%.

The synthesis was performed using a 5% ratio of Tz relative to HA-PD, consistent with the proportion used for HA-Tz synthesis (reported in chapter 4.2.1). However, HA-Tz demonstrated a higher loading capacity of 3.6%. This discrepancy may be attributed to the presence of the previously conjugated PD molecule, which occupies some of the carboxylic groups on the polymer, thereby reducing the availability of these groups for binding with Tz. Additionally, the steric bulk introduced by the PD molecule may interfere with the effective attachment of Tz to HA-PD.

Despite this reduction, the achieved loading capacity of 2.2% was deemed sufficient for subsequent applications. Moreover, it was validated as effective in forming crosslinking between the polymer and PLL-TCO during NPs assembly.

An ^{1}H NMR analysis was conducted on the sample to verify the accuracy of the synthesis and confirm the molecular structure of the obtained product. The resulting spectrum, presented in Figure 24, exhibits all the characteristic peaks associated with the synthesized compound.

- A peak at 2 ppm, integrating for three protons, corresponds to the methyl group protons covalently attached to the polysaccharide backbone;
- the region between 2.8 ppm and 4 ppm reveals a series of overlapping peaks, attributed to the combined signals of the protons from the HA polymer backbone and the protons from the two-carbon alkyl chain present in the PD molecule;
- additionally, distinct peaks are observed in the range of 7.2–8.4 ppm, which are characteristic of the protons from the terminal pyridine ring of the PD component. These signals partially overlap with the aromatic protons of the benzene ring belonging to the Tz moiety.

This detailed spectral analysis confirms the successful conjugation of Tz to the HA-PD polymer chain, validating the intended synthesis steps and providing a foundation for subsequent experiments.

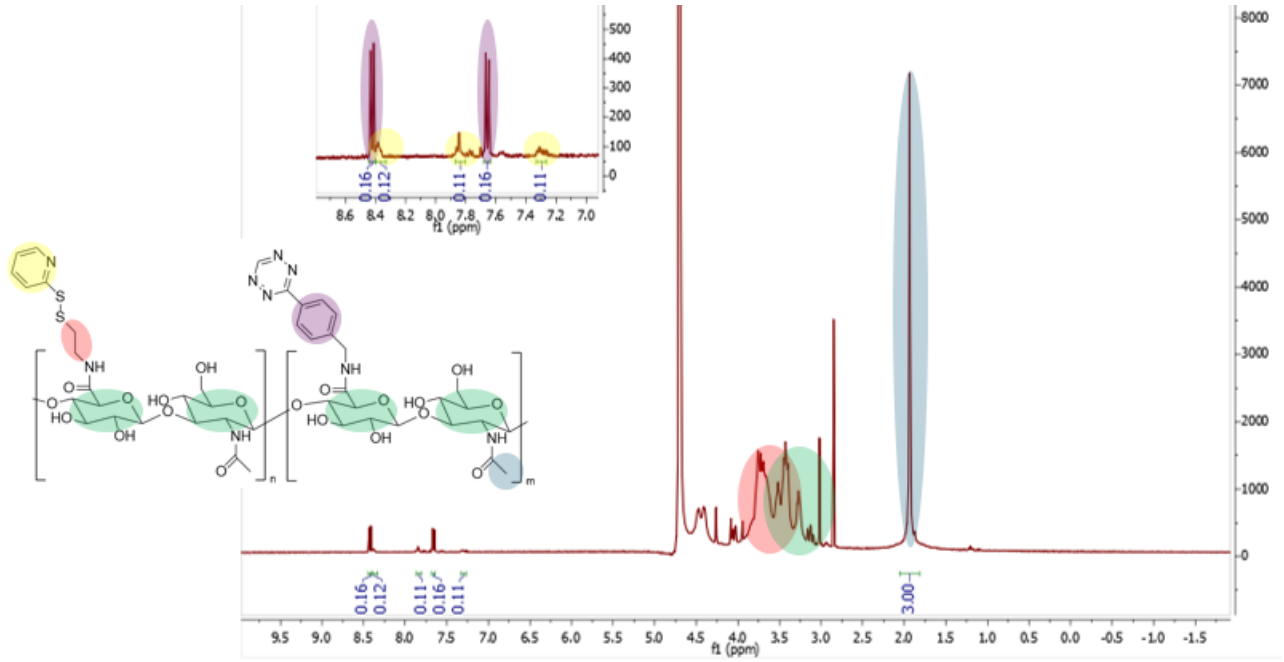

***Figure 24**: [1]H NMR spectrum of HA-PD-Tz in D_2O. Colors on the structure represents the attributed peaks on the spectrum.*

Finally, mass yield of the reaction was calculated, resulted in a 94% yield.

4.3.4. Synthesis and characterization of PTX-SH

To achieve the conjugation of PTX to the HA chain via a disulfide bond, a thiol group was introduced facilitating its covalent conjugation. The hydroxyl group naturally present in the PTX structure served as the anchoring site for the modification. Through this hydroxyl group, mercaptopropionic acid was successfully conjugated to PTX. This reagent was chosen due to its bifunctional nature: it possesses a carboxylic acid group at one end, which was conjugated to PTX hydroxyl group through a Steglich Esterification reaction, and a thiol group at the opposite end, enabling the formation of a disulfide bond with PD.

The synthesis entails the formation of an ester bond linking the hydroxyl group of PTX to the carboxylic group of mercaptopropionic acid. The reaction employs two catalysts to facilitate this transformation: N,N'-dicyclohexylcarbodiimide (DCC) as an activating agent for the carboxylic acid group and 4-dimethylaminopyridine (DMAP) as a nucleophilic catalyst. The reaction mechanism is outlined in the accompanying scheme (*Figure 25*).

In the first step, mercaptopropionic acid is dissolved in the reaction solvent in the presence of DCC, leading to the formation of an O-acylurea intermediate. This intermediate is a reactive species that

significantly enhances the electrophilicity of the carbonyl group, rendering it more susceptible to nucleophilic attack. Next, DMAP is introduced into the reaction mixture. Acting as a nucleophilic catalyst, DMAP interacts with the electrophilic carbonyl center of the O-acylurea intermediate, forming a second, highly reactive intermediate.

The next step involves the addition of PTX. The hydroxyl group of PTX serves as a nucleophile, attacking the electrophilic carbonyl of the activated intermediate. This nucleophilic substitution leads to the formation of a covalent ester bond between PTX and mercaptopropionic acid, achieving the desired functionalization of the drug. The reaction produces N,N'-dicyclohexylurea (DCU) as a by-product, which precipitates from the solution as an insoluble solid. The reaction mixture is filtered under vacuum to remove the solid by-product, followed by precipitation in petroleum ether to eliminate residual impurities.

The final product is lyophilized, yielding a purified material. The synthesized compound was then subjected to comprehensive characterization by elemental analysis, ^{1}H NMR and mass spectrometry to confirm its structure and purity.

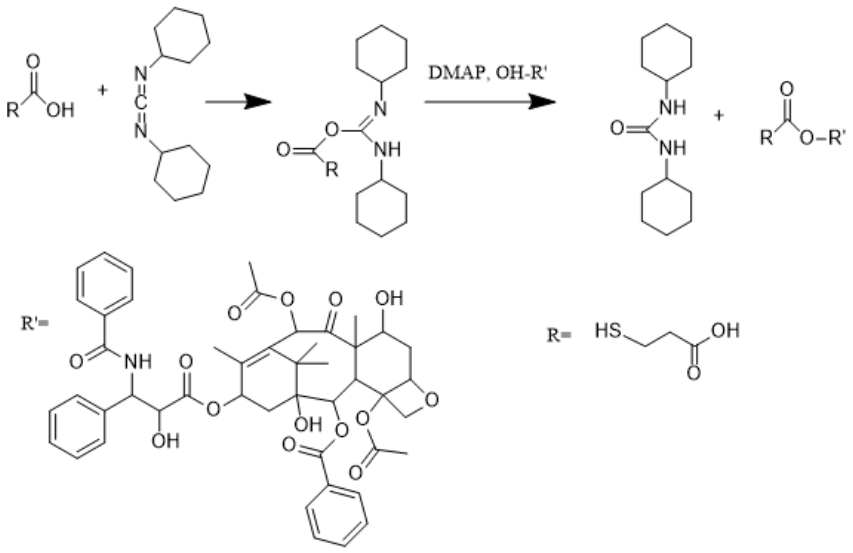

Figure 25*: Scheme of the reaction conducted to link mercaptopropionic acid to PTX using a Steglich Esterification. After the addition of all reagents, the reaction was carried out for one hour in an ice bath, followed by 24 hours at 40 °C*

The results of the elemental analysis for the newly synthesized product confirmed the successful formation of the desired compound, as illustrated in the image below (Figure 26). The elemental composition of the synthesized PTX-SH aligns closely with the calculated theoretical values, supporting the successful outcome of the synthesis. However, as highlighted in the table below, nitrogen is the only element present in a concentration that significantly deviates from the expected values. This anomaly suggests the potential presence of nitrogen-containing residues, contaminants, or impurities within the sample. Moving forward, further efforts will be necessary to optimize the purification process for our product, aiming to identify the source of this discrepancy and implement appropriate corrective measures.

Element	Expected %	Observed %
C	63.750	60.49
H	5.889	6.075
N	1.487	4.925
S	3.404	2.775

***Figure 26**: Results of elemental analysis: comparison between the calculated percentage presence of each element and the experimentally observed value.*

The results of the NMR analysis provide strong evidence that the newly synthesized compound is the desired product. The spectrum, illustrated in Figure 27, reveals several characteristic peaks:

- two peaks at 1.2 ppm integrate for a total of 6 protons, corresponding to the two methyl groups located within the 8-membered ring of the molecule;
- in the region between 7.25 ppm and 8.25 ppm, a cluster of peaks integrates for 15 protons, which can be attributed to the aromatic protons of the three aromatic rings present in the structure of PTX;
- two distinct peaks at 2.15 ppm and 2.25 ppm, each integrating for 2 protons, represent the 4 protons in the alkyl tail conjugated to the PTX molecule during synthesis. These specific signals unequivocally confirm that the synthesis proceeded as intended, with the successful conjugation of mercaptopropionic acid to the PTX molecule.

The successful synthesis of the compound was further verified using mass spectrometry with a negative-mode TOF method. The resulting spectrum revealed a prominent high-intensity peak at

966.3, corresponding to the desired compound. This peak is indicative of the product complexed with a magnesium atom, which is consistent with the negative ionization mode employed in the analysis.

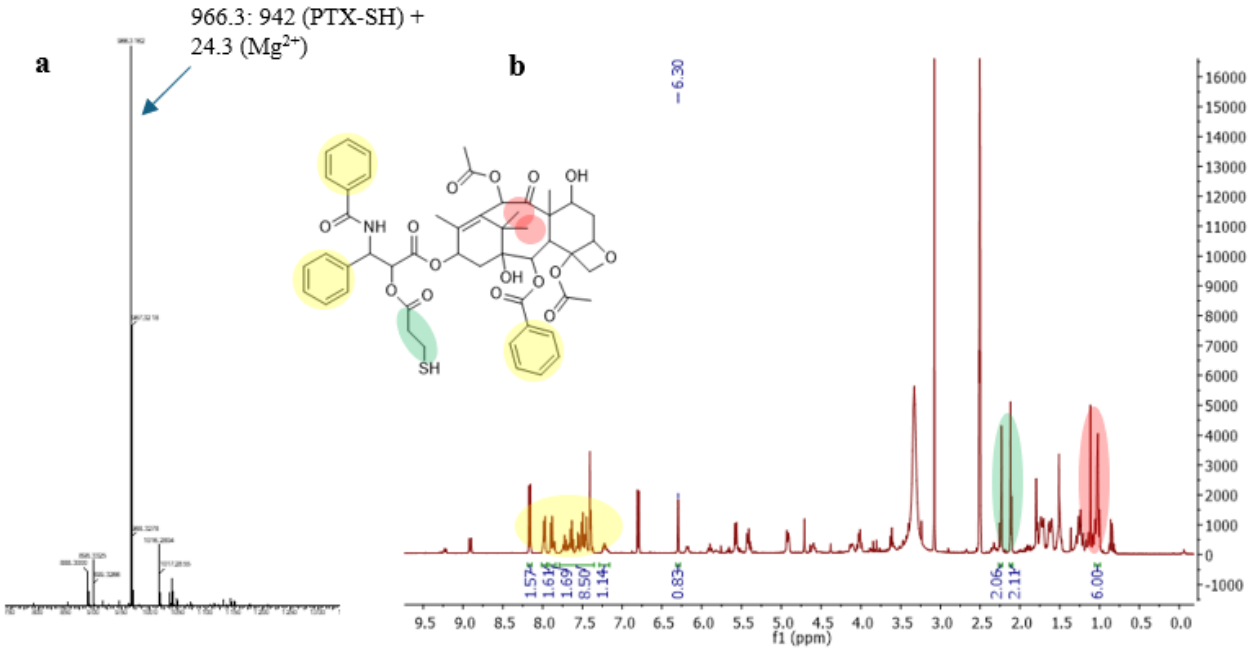

***Figure 27**: MS spectrum of PTX-SH, obtained by TOF method (a) and ^{1}H NMR spectrum of PD (b). Colors on the structure represents the attributed peaks on the spectrum ^{1}H NMR spectrum of PTX-SH in DMSO. Colors in the chemical structure of PTX-SH represent corresponding peaks in the spectrum.*

The molar yield of the reaction was determined to be 49%. Future efforts will focus on optimizing the purification process, to minimize losses and improve the overall yield.

4.3.5. Synthesis and characterization of HA-PD-Tz-PTX

The conjugation of the cytotoxic drug PTX, previously modified in an earlier synthesis step, into the modified HA polymer, constitutes the final stage in the sequence of reactions required to produce an HA polymer tailored to exhibit the desired functionalities. These include the ability to form a bioorthogonal bond with the PLL-TCO polymer chain, a feature provided by the Tz functional group, and the capability to bind PTX via a bioresponsive bond, a property ensured by the presence of PD and PTX-SH.

This final reaction is relatively simple, involving the dissolution of the polymer in water and the drug in DMF, followed by mixing the two solutions and allowing the reaction to proceed under controlled conditions for 24 hours. The product was then purified through precipitation in absolute ethanol and subsequent dialysis to remove impurities. Finally, the purified polymer was lyophilized and subjected to NMR analysis to confirm its structural and chemical properties.

The NMR analysis (reported in Figure 28) provides clear evidence of the successful synthesis, as it exhibits signals attributable to protons from both the polysaccharide chain of modified HA and the PTX molecule. Notable peaks include:

- a signal at 2 ppm corresponding to the methyl group of each monomeric unit in the HA chain;
- a signal at 1.2 ppm associated with the two methyl groups within the 8-membered carbon ring of PTX;
- a series of peaks between 3 ppm and 3.6 ppm attributed to the protons in the HA polysaccharide backbone;
- multiple peaks in the aromatic region between 7 ppm and 8.5 ppm, which represent protons from the three aromatic rings of PTX as well as the aromatic ring in the Tz molecule.

These findings confirm the successful conjugation of PTX to the polymer chain. Furthermore, they validate the accuracy of the preceding synthetic steps, as the final molecule incorporates all the anticipated functional groups derived from the prior reactions.

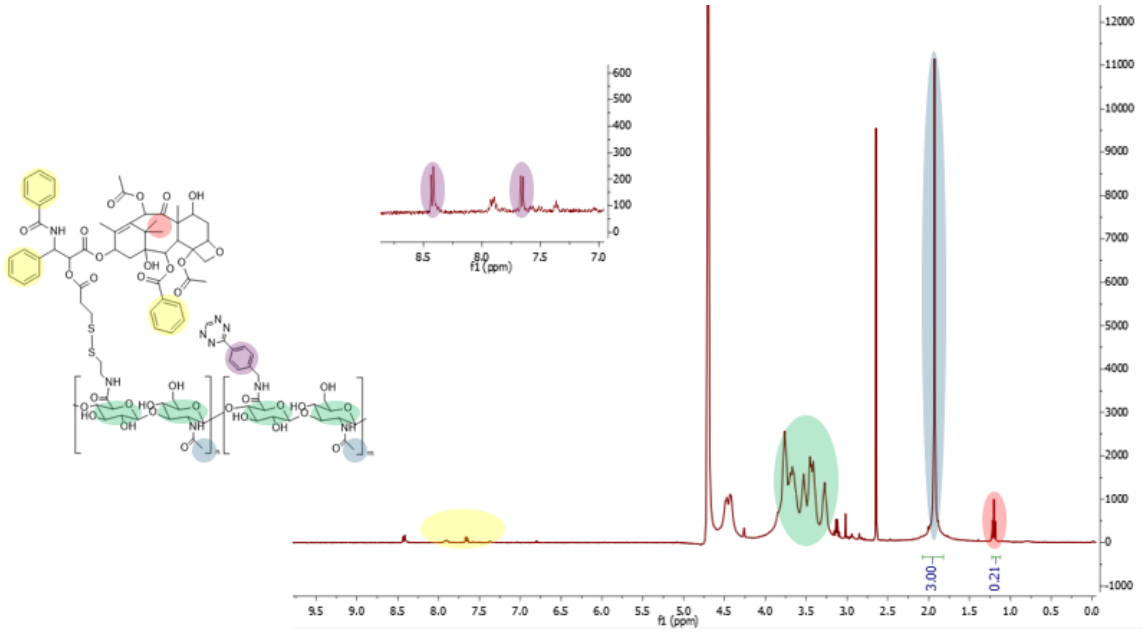

***Figure 28**: [1]H NMR spectrum of HA-PD-Tz-PTZ in D_2O. Colors on the structure represents the attributed peaks on the spectrum.*

A 85% mass yield of the reaction was finally calculated.

4.3.6. Formulation and characterization of CL HAPLL NPs-PTX

Following the successful synthesis and characterization of the HA-PD-Tz-PTX conjugate, its corresponding NPs were formulated. Taking advantage of the promising results obtained during the

scale-up of drug-free crosslinked NPs, the same formulation strategy and polymer ratio were applied. Specifically, NPs were prepared using an HA-to-PLL weight ratio of 10:1. Using microfluidic technology, 15 mL of a 5 mg/mL solution of the modified HA polymer was mixed with 15 mL of a 0.5 mg/mL solution of PLL-TCO polymer, yielding a solution of CL HAPLL NPs-PTX.

The design of these NPs necessitates the assurance of key fundamental properties to ensure their therapeutic potential and to support their advancement toward clinical application. Foremost among these is their stability within a physiological environment, which must be maintained both immediately after intracranial administration and throughout their retention within the brain parenchyma. This stability is vital to preserve their structural and functional integrity under in vivo conditions. Additionally, their size plays a pivotal role in determining their capacity to penetrate brain tissue and diffuse within the glioblastoma microenvironment. To effectively target deeper tumor regions, nanoparticles must exhibit a precisely controlled size. An average size of approx. 100 nm is particularly favorable, as it balances diffusion efficiency and tissue penetration, allowing the particles to traverse the tumor mass and deliver therapeutic agents to otherwise inaccessible areas.

For this reason, DLS was used to assess the size of the CL HAPLL NPs-PTX, initially in water and subsequently in PBS, to evaluate their stability in aqueous and saline environments. The CL HAPLL NPs-PTX exhibited a size of 250 nm, which remained unchanged in PBS as shown in *Figure 29*, indicating excellent stability under physiological conditions. This stability is crucial, ensuring that the NPs retain their functional integrity in biological environments without disassembling.

However, the size in both in water and in PBS increase compared to drug-free NPs (approximately 50 nm) highlights the substantial impact of PTX and its linker on the final NPs dimensions. This result aligns with expectations, as PTX is a large, hydrophobic molecule that avoids aqueous environments, leading the hydrophilic polymer to envelop and shield it from the external medium.

Literature suggests that particle sizes below 100 nm are optimal for effective diffusion within GBM tissues[112]. Nevertheless, we hypothesize that the larger size of our NPs may still permit efficient infiltration into the brain parenchyma. Unlike the rigid systems commonly reported in the literature, our polymeric NPs exhibit a flexible and fluffy structure, enabling them to adapt their shape and pass through pores smaller than their nominal diameter.

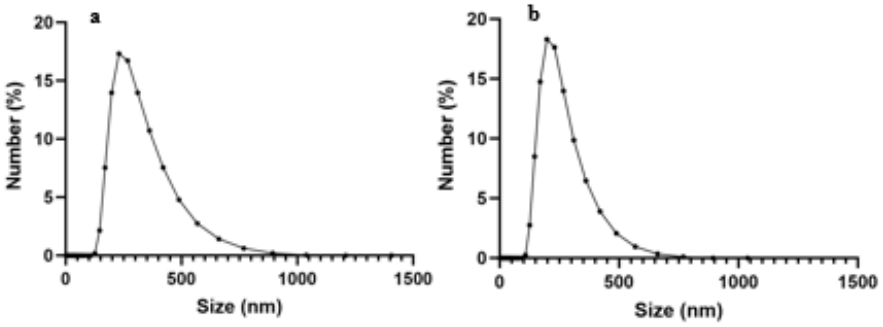

***Figure 29**: DLS analysis of NPs-PTX conducted in water (a) and in PBS (b), showing the stability of the NPs in different solvents*

A stability study was subsequently conducted on the CL HAPLL NPs-PTX, involving the preparation of three different solutions. The first solution was in PBS and stored at 4°C for 72 hours, while the second and third solutions were prepared in CSF and PBS, respectively, and maintained at 37°C for 72 hours. All solutions were periodically analyzed at regular intervals (0, 24, 48, and 72 hours). As illustrated in *Figure 30*, the CL HAPLL NPs-PTXexhibited a highly stability profile, which is a critical attribute for their prospective clinical applications.

The observed stability at 4°C suggests that, in a clinical setting, the CL HAPLL NPs-PTX could be stored in a refrigerated state after suspension in a physiological solution at the time of patient administration. This would enable the preservation of unused material, reducing waste. Additionally, their stability at 37°C demonstrates their capacity to maintain their structural integrity and essential properties after intracranial injection, ensuring proper diffusion and sustained functionality for at least 72 hours. This attribute is particularly important for maintaining therapeutic efficacy within the target environment.

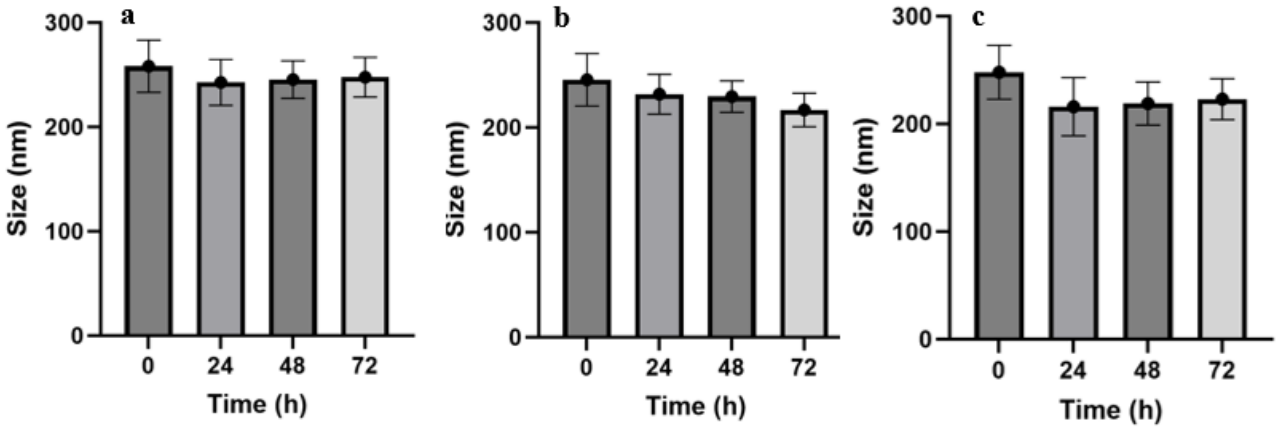

***Figure 30**: Stability study of CL NPs in different solvents: a) PBS at 4 °C, b) CSF at 37 °C, c) PBS at 37 °C proving the stability properties of CL NPs*

The morphology and size of the CL HAPLL NPs-PTX were further characterized using TEM analysis. This technique revealed an average particle size of approximately 200 nm, which is slightly smaller than the size obtained from DLS measurements. The discrepancy can be explained by the nature of the two techniques: TEM analysis involves the drying of the sample, which removes the aqueous component inherently associated with the particles and is included in the size measurement during DLS analysis conducted in an aqueous medium. The drying process may cause the polymer matrix to shrink, resulting in smaller observed dimensions.

Although Cryo-TEM would offer a more precise evaluation by preserving the hydrated state of the nanoparticles, this method was not available for the current study. Nevertheless, the TEM analysis provided critical insights, confirming that the nanoparticles have a size consistent with expectations and exhibit a spherical morphology as anticipated. Results obtained by TEM analysis are shown in *Figure 31*.

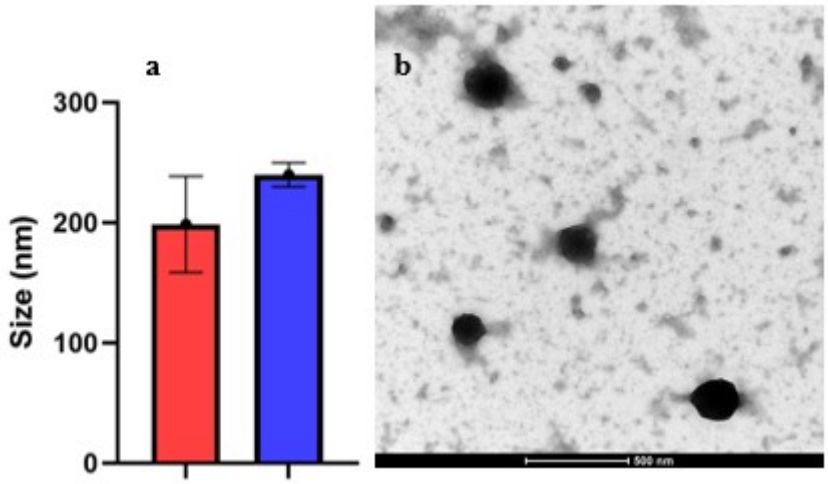

***Figure 31**: CL HAPLL NPs-PTX size obtained with TEM analysis (red) and DLS analysis (blue) (a) and morphology obtained with TEM analysis (b). Scale bar is 500 nm..*

5. Conclusions and perspectives

GBM represents one of the most significant unmet clinical challenges, largely due to its complex nature and resistance to conventional therapies. The difficulty in achieving an effective treatment stems from several intrinsic characteristics of GBM, including its pronounced inter- and intra-tumoral heterogeneity, its anatomical position, which shields it from systemically administered drugs via the BBB, its aggressive proliferative and invasive behavior, and its ability to develop robust chemoresistance mechanisms.

This project aimed to address these barriers by focusing on the design, synthesis and characterization of polymer-based NPs conjugated to a chemotherapeutic agent, specifically for localized GBM therapy. Localized delivery bypasses the BBB, avoiding the associated challenges and allowing for the achievement of therapeutic drug concentrations directly at the tumor site. The polymer-based nature of these NPs confers significant advantages, including biocompatibility, biodegradability and active targeting of GBM cells, thereby reducing off-target toxicity to healthy neural tissues.

We developed NPs by chemically modifying HA and PLL to enable covalent crosslinking. The resulting bioorthogonal linking chemistry provided stability to the NPs structure, even in challenging physiological environments. The resulting NPs resulted in a size of 50 nm, zeta potential of -50 mV and negligible toxicity on murine GBM cells. These findings underscore the potential of these crosslinked polymeric nanoparticles as a promising platform for localized glioblastoma therapy. After successfully formulating these promising NPs, efforts were directed towards conjugating them with a chemotherapeutic drug, PTX. To enhance therapeutic efficacy and ensure precise drug delivery, a strategy was devised to enable the controlled release of PTX selectively within tumor cells. The formulated NPs not only meet the desired specifications of controlled dimensions but also effectively conjugate the drug through a bioresponsive disulfide bond. Additionally, they exhibit excellent stability in physiological environments and retain their properties over extended periods, making them a promising candidate for future applications in glioblastoma therapy.

However, several aspects of the project require further refinement and investigation. A key challenge is improving the reaction yield for the synthesis of PTX-SH, as the current method has not yet achieved a satisfactory outcome. Optimizing this step will be crucial for ensuring the reproducibility and efficiency of the process.

Future efforts will also focus on the accurate quantification of PTX effectively conjugated to the NPs. Although attempts were made during this project using HPLC for quantification, the results were

suboptimal due to the inability to operate under ideal conditions. Further method optimization and validation will be prioritized in subsequent studies.

Another critical area of exploration will be the evaluation of the drug release profile of the NPs-PTX in a reducing environment. This study will provide essential insights into their controlled release behavior under conditions that mimic the glioblastoma microenvironment. Following this, a comprehensive cell viability analysis will be conducted on the SB28 cells. The experimental design for these studies will consider the IC_{50} of PTX, the drug concentration within the nanoparticles and its release kinetics, ensuring a precise and clinically relevant evaluation. Cell uptake studies and the mechanism of cell trafficking need to be studied using flow cytometry and confocal microscopy analysis.

Finally, in vivo studies will be conducted. The mechanism of HAPLL NP-PTX diffusion through the tumor mass warrants further examination. Whether the NPs migrate via transcellular or paracellular pathways remains to be definitively established. Preliminary data from our research group suggest that both mechanisms may contribute to their movement, but these hypotheses require rigorous experimental validation. Understanding this behavior will be pivotal for optimizing the therapeutic efficacy of the nanoparticle system and enhancing its potential for clinical application.

6. References

1. Weller, M., et al., *Glioma.* Nature reviews Disease primers, 2015. **1**(1): p. 1-18.
2. Wiestler, B., et al., *Multiparametric MRI-based differentiation of WHO grade II/III glioma and WHO grade IV glioblastoma.* Scientific reports, 2016. **6**(1): p. 35142.
3. Blissitt, P.A., *Clinical practice guideline series update: care of the adult patient with a brain tumor.* Journal of Neuroscience Nursing, 2014. **46**(6): p. 367-368.
4. Kleihues, P. and H. Ohgaki, *Primary and secondary glioblastomas: from concept to clinical diagnosis.* Neuro-oncology, 1999. **1**(1): p. 44-51.
5. Stoyanov, G.S., et al., *Reclassification of glioblastoma multiforme according to the 2021 World Health Organization classification of central nervous system tumors: a single institution report and practical significance.* Cureus, 2022. **14**(2).
6. Thakkar, J.P., et al., *Epidemiologic and molecular prognostic review of glioblastoma.* Cancer epidemiology, biomarkers & prevention, 2014. **23**(10): p. 1985-1996.
7. Ohgaki, H. and P. Kleihues, *The definition of primary and secondary glioblastoma.* Clinical cancer research, 2013. **19**(4): p. 764-772.
8. Stupp, R., et al., *High-grade glioma: ESMO Clinical Practice Guidelines for diagnosis, treatment and follow-up.* Annals of oncology, 2014. **25**: p. iii93-iii101.
9. Ganipineni, L.P., et al., *Magnetic targeting of paclitaxel-loaded poly (lactic-co-glycolic acid)-based nanoparticles for the treatment of glioblastoma.* International journal of nanomedicine, 2018: p. 4509-4521.
10. Mrugala, M.M., *Advances and challenges in the treatment of glioblastoma: a clinician's perspective.* Discovery medicine, 2013. **15**(83): p. 221-230.
11. Adegboyega, G., et al., *Global landscape of glioblastoma multiforme management in the stupp protocol era: systematic review protocol.* International Journal of Surgery Protocols, 2021. **25**(1): p. 108-113.
12. Zhang, J., M. FG Stevens, and T. D Bradshaw, *Temozolomide: mechanisms of action, repair and resistance.* Current molecular pharmacology, 2012. **5**(1): p. 102-114.
13. Jacinto, F.V. and M. Esteller, *MGMT hypermethylation: a prognostic foe, a predictive friend.* DNA repair, 2007. **6**(8): p. 1155-1160.
14. Da Ros, M., et al., *Glioblastoma chemoresistance: The double play by microenvironment and blood-brain barrier.* International journal of molecular sciences, 2018. **19**(10): p. 2879.
15. Bausart, M., V. Préat, and A. Malfanti, *Immunotherapy for glioblastoma: the promise of combination strategies.* Journal of Experimental & Clinical Cancer Research, 2022. **41**(1): p. 35.
16. Jezierzański, M., et al., *Temozolomide (TMZ) in the treatment of glioblastoma multiforme—A literature review and clinical outcomes.* Current Oncology, 2024. **31**(7): p. 3994-4002.
17. Ahmed, M., et al., *Role of multidrug resistance in glioblastoma chemoresistance: Focus on ABC transporters.* Glioblastoma resistance to chemotherapy: molecular mechanisms and innovative reversal strategies, 2021: p. 243-261.
18. Persano, L., et al., *Glioblastoma cancer stem cells: role of the microenvironment and therapeutic targeting.* Biochemical pharmacology, 2013. **85**(5): p. 612-622.
19. Uribe, D., et al., *Multidrug resistance in glioblastoma stem-like cells: Role of the hypoxic microenvironment and adenosine signaling.* Molecular aspects of medicine, 2017. **55**: p. 140-151.
20. Singh, N., et al., *Mechanisms of temozolomide resistance in glioblastoma-a comprehensive review.* Cancer drug resistance, 2021. **4**(1): p. 17.
21. Rivera, A.L., et al., *MGMT promoter methylation is predictive of response to radiotherapy and prognostic in the absence of adjuvant alkylating chemotherapy for glioblastoma.* Neuro-oncology, 2010. **12**(2): p. 116-121.

22. Abbott, N.J., et al., *Structure and function of the blood–brain barrier.* Neurobiology of disease, 2010. **37**(1): p. 13-25.
23. Yu, M.W. and D.F. Quail, *Immunotherapy for glioblastoma: current progress and challenges.* Frontiers in immunology, 2021. **12**: p. 676301.
24. Pardridge, W.M., *Drug transport across the blood–brain barrier.* Journal of cerebral blood flow & metabolism, 2012. **32**(11): p. 1959-1972.
25. Sprowls, S.A., et al., *Improving CNS delivery to brain metastases by blood–tumor barrier disruption.* Trends in cancer, 2019. **5**(8): p. 495-505.
26. Wolburg, H., et al., *Localization of claudin-3 in tight junctions of the blood-brain barrier is selectively lost during experimental autoimmune encephalomyelitis and human glioblastoma multiforme.* Acta neuropathologica, 2003. **105**: p. 586-592.
27. Sarkaria, J.N., et al., *Is the blood–brain barrier really disrupted in all glioblastomas? A critical assessment of existing clinical data.* Neuro-oncology, 2018. **20**(2): p. 184-191.
28. Ohgaki, H., et al., *Genetic pathways to glioblastoma: a population-based study.* Cancer research, 2004. **64**(19): p. 6892-6899.
29. Ohgaki, H. and P. Kleihues, *Genetic pathways to primary and secondary glioblastoma.* The American journal of pathology, 2007. **170**(5): p. 1445-1453.
30. Purow, B. and D. Schiff, *Advances in the genetics of glioblastoma: are we reaching critical mass?* Nature Reviews Neurology, 2009. **5**(8): p. 419-426.
31. Stoyanov, G.S., et al., *The Rapid Development of Glioblastoma: A Report of Two Cases.* Cureus, 2022. **14**(6).
32. Gan, X., Y. Liu, and X. Wang, *Targeting androgen receptor in glioblastoma.* Critical Reviews in Oncology/Hematology, 2023. **191**: p. 104142.
33. Watanabe, K., et al., *Overexpression of the EGF receptor and p53 mutations are mutually exclusive in the evolution of primary and secondary glioblastomas.* Brain pathology, 1996. **6**(3): p. 217-223.
34. Hollstein, M., et al., *p53 mutations in human cancers.* Science, 1991. **253**(5015): p. 49-53.
35. Biernat, W., et al., *Amplification and overexpression of MDM2 in primary (de novo) glioblastomas.* Journal of Neuropathology & Experimental Neurology, 1997. **56**(2): p. 180-185.
36. Koul, D., *PTEN signaling pathways in glioblastoma.* Cancer biology & therapy, 2008. **7**(9): p. 1321-1325.
37. Parsons, D.W., et al., *An integrated genomic analysis of human glioblastoma multiforme.* science, 2008. **321**(5897): p. 1807-1812.
38. Saxena, A., et al., *Comparative molecular genetic profiles of anaplastic astrocytomas/glioblastomas multiforme and their subsequent recurrences.* Oncogene, 1999. **18**(6): p. 1385-1390.
39. 1, C.G.A.R.N.T.s.s.D.U.M.S.M.R.F.A.B.D., et al., *Comprehensive genomic characterization defines human glioblastoma genes and core pathways.* Nature, 2008. **455**(7216): p. 1061-1068.
40. Liu, W., et al., *PTEN/MMAC1 mutations and EGFR amplification in glioblastomas.* Cancer research, 1997. **57**(23): p. 5254-5257.
41. Serrano, M., G.J. Hannon, and D. Beach, *A new regulatory motif in cell-cycle control causing specific inhibition of cyclin D/CDK4.* nature, 1993. **366**(6456): p. 704-707.
42. Reifenberger, G., et al., *Amplification of multiple genes from chromosomal region 12q13-14 in human malignant gliomas: preliminary mapping of the amplicons shows preferential involvement of CDK4, SAS, and MDM2.* Cancer research, 1994. **54**(16): p. 4299-4303.
43. Davis, M.E., *Glioblastoma: overview of disease and treatment.* Clinical journal of oncology nursing, 2016. **20**(5): p. S2.

44. Segerman, A., et al., *Clonal variation in drug and radiation response among glioma-initiating cells is linked to proneural-mesenchymal transition.* Cell reports, 2016. **17**(11): p. 2994-3009.
45. Baghban, R., et al., *Tumor microenvironment complexity and therapeutic implications at a glance.* Cell Communication and Signaling, 2020. **18**: p. 1-19.
46. Qian, J., et al., *TLR2 promotes glioma immune evasion by downregulating MHC class II molecules in microglia.* Cancer Immunology Research, 2018. **6**(10): p. 1220-1233.
47. Himes, B.T., et al., *Immunosuppression in glioblastoma: current understanding and therapeutic implications.* Frontiers in oncology, 2021. **11**: p. 770561.
48. Wilmotte, R., et al., *B7-homolog 1 expression by human glioma: a new mechanism of immune evasion.* Neuroreport, 2005. **16**(10): p. 1081-1085.
49. Tchirkov, A., et al., *IL-6 gene amplification and expression in human glioblastomas.* British journal of cancer, 2001. **85**(4): p. 518-522.
50. Chen, Z., et al., *Cellular and molecular identity of tumor-associated macrophages in glioblastoma.* Cancer research, 2017. **77**(9): p. 2266-2278.
51. Raber, P.L., et al., *Subpopulations of myeloid-derived suppressor cells impair T cell responses through independent nitric oxide-related pathways.* International journal of cancer, 2014. **134**(12): p. 2853-2864.
52. Wainwright, D.A., et al., *IDO expression in brain tumors increases the recruitment of regulatory T cells and negatively impacts survival.* Clinical cancer research, 2012. **18**(22): p. 6110-6121.
53. Rodrigues, J.C., et al., *Normal human monocytes exposed to glioma cells acquire myeloid-derived suppressor cell-like properties.* Neuro-oncology, 2010. **12**(4): p. 351-365.
54. Takeuchi, Y. and H. Nishikawa, *Roles of regulatory T cells in cancer immunity.* International immunology, 2016. **28**(8): p. 401-409.
55. Gimple, R.C., et al., *Glioblastoma stem cells: lessons from the tumor hierarchy in a lethal cancer.* Genes & development, 2019. **33**(11-12): p. 591-609.
56. Bozzato, E., C. Bastiancich, and V. Préat, *Nanomedicine: A useful tool against glioma stem cells.* Cancers, 2020. **13**(1): p. 9.
57. Teng, J., et al., *Dissecting inherent intratumor heterogeneity in patient-derived glioblastoma culture models.* Neuro-oncology, 2017. **19**(6): p. 820-832.
58. Badr, C.E., et al., *Metabolic heterogeneity and adaptability in brain tumors.* Cellular and Molecular Life Sciences, 2020. **77**: p. 5101-5119.
59. Lathia, J.D., et al., *Cancer stem cells in glioblastoma.* Genes & development, 2015. **29**(12): p. 1203-1217.
60. Di Tomaso, T., et al., *Immunobiological characterization of cancer stem cells isolated from glioblastoma patients.* Clinical Cancer Research, 2010. **16**(3): p. 800-813.
61. Haar, C.P., et al., *Drug resistance in glioblastoma: a mini review.* Neurochemical research, 2012. **37**: p. 1192-1200.
62. Smith, A.G. and K.F. Macleod, *Autophagy, cancer stem cells and drug resistance.* The Journal of pathology, 2019. **247**(5): p. 708-718.
63. Dubois, L.G., et al., *Gliomas and the vascular fragility of the blood brain barrier.* Frontiers in cellular neuroscience, 2014. **8**: p. 418.
64. Monteiro, A.R., et al., *The role of hypoxia in glioblastoma invasion.* Cells, 2017. **6**(4): p. 45.
65. Brown, T.J., et al., *Association of the extent of resection with survival in glioblastoma: a systematic review and meta-analysis.* JAMA oncology, 2016. **2**(11): p. 1460-1469.
66. Burger, P.C., et al., *Topographic anatomy and CT correlations in the untreated glioblastoma multiforme.* Journal of neurosurgery, 1988. **68**(5): p. 698-704.
67. van Solinge, T.S., et al., *Advances in local therapy for glioblastoma—taking the fight to the tumour.* Nature Reviews Neurology, 2022. **18**(4): p. 221-236.

68. Chua, C.Y.X., et al., *Emerging technologies for local cancer treatment.* Advanced therapeutics, 2020. **3**(9): p. 2000027.
69. Vogelbaum, M.A. and M.K. Aghi, *Convection-enhanced delivery for the treatment of glioblastoma.* Neuro-oncology, 2015. **17**(suppl_2): p. ii3-ii8.
70. Cha, G.D., et al., *Advances in drug delivery technology for the treatment of glioblastoma multiforme.* Journal of Controlled Release, 2020. **328**: p. 350-367.
71. Mehta, A., A. Sonabend, and J. Bruce, *Convection-enhanced delivery.* Neurotherapeutics, 2017. **14**(2): p. 358-371.
72. Jahangiri, A., et al., *Convection-enhanced delivery in glioblastoma: a review of preclinical and clinical studies.* Journal of neurosurgery, 2017. **126**(1): p. 191-200.
73. Yeini, E., et al., *Targeting glioblastoma: Advances in drug delivery and novel therapeutic approaches.* Advanced Therapeutics, 2021. **4**(1): p. 2000124.
74. Westphal, M., et al., *A phase 3 trial of local chemotherapy with biodegradable carmustine (BCNU) wafers (Gliadel wafers) in patients with primary malignant glioma.* Neuro-oncology, 2003. **5**(2): p. 79-88.
75. Gazaille, C., et al., *Local delivery and glioblastoma: why not combining sustained release and targeting?* Frontiers in Medical Technology, 2021. **3**: p. 791596.
76. Kirson, E.D., et al., *Disruption of cancer cell replication by alternating electric fields.* Cancer research, 2004. **64**(9): p. 3288-3295.
77. Rick, J., A. Chandra, and M.K. Aghi, *Tumor treating fields: a new approach to glioblastoma therapy.* Journal of Neuro-Oncology, 2018. **137**: p. 447-453.
78. Fabian, D., et al., *Treatment of glioblastoma (GBM) with the addition of tumor-treating fields (TTF): a review.* Cancers, 2019. **11**(2): p. 174.
79. Foo, C.Y., et al., *Medical device advances in the treatment of glioblastoma.* Cancers, 2022. **14**(21): p. 5341.
80. Chiocca, E.A., et al., *Viral and other therapies for recurrent glioblastoma: is a 24-month durable response unusual?* Neuro-oncology, 2019. **21**(1): p. 14-25.
81. Stepanenko, A.A. and V.P. Chekhonin, *Recent advances in oncolytic virotherapy and immunotherapy for glioblastoma: a glimmer of hope in the search for an effective therapy?* Cancers, 2018. **10**(12): p. 492.
82. Maggs, L., et al., *CAR T cell-based immunotherapy for the treatment of glioblastoma.* Frontiers in neuroscience, 2021. **15**: p. 662064.
83. Migliorini, D., et al., *CAR T-cell therapies in glioblastoma: a first look.* Clinical Cancer Research, 2018. **24**(3): p. 535-540.
84. Kim, B.Y., J.T. Rutka, and W.C. Chan, *Nanomedicine.* New England Journal of Medicine, 2010. **363**(25): p. 2434-2443.
85. Shi, J., et al., *Cancer nanomedicine: progress, challenges and opportunities.* Nature reviews cancer, 2017. **17**(1): p. 20-37.
86. Ananda, S., et al., *Phase 2 trial of temozolomide and pegylated liposomal doxorubicin in the treatment of patients with glioblastoma multiforme following concurrent radiotherapy and chemotherapy.* Journal of Clinical Neuroscience, 2011. **18**(11): p. 1444-1448.
87. Lim, K.J., et al., *A polymeric nanoparticle formulation of curcumin inhibits growth, clonogenicity and stem-like fraction in malignant brain tumors.* Cancer biology & therapy, 2011. **11**(5): p. 464-473.
88. Zanotto-Filho, A., et al., *Curcumin-loaded lipid-core nanocapsules as a strategy to improve pharmacological efficacy of curcumin in glioma treatment.* European Journal of Pharmaceutics and Biopharmaceutics, 2013. **83**(2): p. 156-167.
89. Jnaidi, R., A.J. Almeida, and L.M. Gonçalves, *Solid lipid nanoparticles and nanostructured lipid carriers as smart drug delivery systems in the treatment of glioblastoma multiforme.* Pharmaceutics, 2020. **12**(9): p. 860.

90. Basso, J., et al., *Hydrogel-based drug delivery nanosystems for the treatment of brain tumors.* Gels, 2018. **4**(3): p. 62.
91. Pinel, S., et al., *Approaches to physical stimulation of metallic nanoparticles for glioblastoma treatment.* Advanced drug delivery reviews, 2019. **138**: p. 344-357.
92. Dwivedi, N., et al., *Dendrimer-mediated approaches for the treatment of brain tumor.* Journal of Biomaterials science, Polymer edition, 2016. **27**(7): p. 557-580.
93. Paldor, I., et al., *Targeted local therapy for management of intracranial high-grade gliomas.* Intracranial Gliomas Part III-Innovative Treatment Modalities, 2018. **32**: p. 159-171.
94. Din, F.U., et al., *Effective use of nanocarriers as drug delivery systems for the treatment of selected tumors.* International journal of nanomedicine, 2017: p. 7291-7309.
95. Duncan, R. and M.J. Vicent, *Polymer therapeutics-prospects for 21st century: the end of the beginning.* Advanced drug delivery reviews, 2013. **65**(1): p. 60-70.
96. Duncan, R., *Development of HPMA copolymer–anticancer conjugates: clinical experience and lessons learnt.* Advanced drug delivery reviews, 2009. **61**(13): p. 1131-1148.
97. Dhal, P.K., et al., *Functional polymers as therapeutic agents: concept to market place.* Advanced drug delivery reviews, 2009. **61**(13): p. 1121-1130.
98. Sanchis, J., et al., *Polymer–drug conjugates for novel molecular targets.* Nanomedicine, 2010. **5**(6): p. 915-935.
99. Loftus, J.V., et al., *Changes in vision-and health-related quality of life in patients with diabetic macular edema treated with pegaptanib sodium or sham.* Investigative ophthalmology & visual science, 2011. **52**(10): p. 7498-7505.
100. Alphandéry, E., et al., *Cancer therapy using nanoformulated substances: scientific, regulatory and financial aspects.* Expert Review of anticancer therapy, 2015. **15**(10): p. 1233-1255.
101. Wolinsky, J.B. and M.W. Grinstaff, *Therapeutic and diagnostic applications of dendrimers for cancer treatment.* Advanced drug delivery reviews, 2008. **60**(9): p. 1037-1055.
102. Jeyapalan, S., et al., *Paclitaxel poliglumex, temozolomide, and radiation for newly diagnosed high-grade glioma: a Brown University Oncology Group Study.* American journal of clinical oncology, 2014. **37**(5): p. 444-449.
103. Duncan, R. and S.C. Richardson, *Endocytosis and intracellular trafficking as gateways for nanomedicine delivery: opportunities and challenges.* Molecular pharmaceutics, 2012. **9**(9): p. 2380-2402.
104. Webster, R., et al., *PEG and PEG conjugates toxicity: towards an understanding of the toxicity of PEG and its relevance to PEGylated biologicals.* PEGylated protein drugs: Basic science and clinical applications, 2009: p. 127-146.
105. Rathore, A.S., *Roadmap for implementation of quality by design (QbD) for biotechnology products.* Trends in biotechnology, 2009. **27**(9): p. 546-553.
106. Bastiancich, C., et al., *Rationally designed drug delivery systems for the local treatment of resected glioblastoma.* Advanced drug delivery reviews, 2021. **177**: p. 113951.
107. Šamec, N., et al., *Nanomedicine and immunotherapy: a step further towards precision medicine for glioblastoma.* Molecules, 2020. **25**(3): p. 490.
108. Brem, S., et al., *Local delivery of temozolomide by biodegradable polymers is superior to oral administration in a rodent glioma model.* Cancer chemotherapy and pharmacology, 2007. **60**: p. 643-650.
109. Cai, Q., et al., *Systemic delivery to central nervous system by engineered PLGA nanoparticles.* American journal of translational research, 2016. **8**(2): p. 749.
110. Yoo, J., et al., *Active targeting strategies using biological ligands for nanoparticle drug delivery systems.* Cancers, 2019. **11**(5): p. 640.
111. Wang, S., et al., *Receptor-mediated drug delivery systems targeting to glioma.* Nanomaterials, 2015. **6**(1): p. 3.

112. Nance, E., et al., *Brain-penetrating nanoparticles improve paclitaxel efficacy in malignant glioma following local administration.* ACS nano, 2014. **8**(10): p. 10655-10664.
113. Zhao, M., et al., *Codelivery of paclitaxel and temozolomide through a photopolymerizable hydrogel prevents glioblastoma recurrence after surgical resection.* Journal of controlled release, 2019. **309**: p. 72-81.
114. Dicker, K.T., et al., *Hyaluronan: a simple polysaccharide with diverse biological functions.* Acta biomaterialia, 2014. **10**(4): p. 1558-1570.
115. Kim, Y. and S. Kumar, *CD44-mediated adhesion to hyaluronic acid contributes to mechanosensing and invasive motility.* Molecular Cancer Research, 2014. **12**(10): p. 1416-1429.
116. Chellen, T., et al., *In situ administration of STING-activating hyaluronic acid conjugate primes anti-glioblastoma immune response.* Materials Today Bio, 2024. **26**: p. 101057.
117. Catania, G., et al., *Combination of hyaluronic acid conjugates with immunogenic cell death inducer and CpG for glioblastoma local chemo-immunotherapy elicits an immune response and induces long-term survival.* Biomaterials, 2023. **294**: p. 122006.
118. Malfanti, A., et al., *Design of bio-responsive hyaluronic acid–doxorubicin conjugates for the local treatment of glioblastoma.* Pharmaceutics, 2022. **14**(1): p. 124.
119. Su, Y., et al., *Roles of arginine and lysine residues in the translocation of a cell-penetrating peptide from 13C, 31P, and 19F solid-state NMR.* Biochemistry, 2009. **48**(21): p. 4587-4595.
120. Qiao, Z., et al., *Host defense peptide-mimicking peptide polymer-based antibacterial hydrogel enables efficient healing of MRSA-infected wounds.* Science China Chemistry, 2023. **66**(6): p. 1824-1833.
121. Ganipineni, L.P., F. Danhier, and V. Préat, *Drug delivery challenges and future of chemotherapeutic nanomedicine for glioblastoma treatment.* Journal of controlled release, 2018. **281**: p. 42-57.
122. McConnell, H., J. Bianchine, and A. Wilder-Smith, *Composition of CSF*, in *Cerebrospinal Fluid in Neurology and Psychiatry*. 1994, Springer. p. 57-109.
123. Medicago, A., *Phosphate Buffered Saline (PBS), pH 7.4 and 7.2.* URl: http://www. medicago. se/sites/default/files/pdf/productsheets/PBS_Buffer_v. _01. pdf.(accessed: 01.01. 2021), 2021.
124. Stéen, E.J.L., et al., *Trans-cyclooctene-functionalized peptobrushes with improved reaction kinetics of the tetrazine ligation for pretargeted nuclear imaging.* ACS nano, 2019. **14**(1): p. 568-584.
125. Horwitz, S., *Taxol (paclitaxel): mechanisms of action.* Annals of oncology: official journal of the European Society for Medical Oncology, 1994. **5**: p. S3-6.
126. Zhan, C., et al., *Co-delivery of TRAIL gene enhances the anti-glioblastoma effect of paclitaxel in vitro and in vivo.* Journal of controlled release, 2012. **160**(3): p. 630-636.